

Modelling coarse and giant desert dust particles

Eleni Drakaki^{1,2}, Vassilis Amiridis¹, Alexandra Tsekeri¹, Antonis Gkikas¹, Emmanouil Proestakis¹, Sotirios Mallios¹, Stavros Solomos³, Christos Spyrou¹, Eleni Marinou^{1,4}, Claire L. Ryder⁵, Demetri Bouris⁶, and Petros Katsafados²

¹IAASARS, National Observatory of Athens, Athens GR-15236, Greece

²Harokopion University of Athens (HUA), Department of Geography, Athens GR-17671, Greece

³Academy of Athens, Research Centre for Atmospheric Physics and Climatology, Athens GR-10679, Greece

⁴Institut für Physik der Atmosphäre, Deutsches Zentrum für Luft- und Raumfahrt, Oberpfaffenhofen, Germany

⁵University of Reading, Department of Meteorology, Reading, RG6 6BB, UK

⁶National Technical University of Athens, School of Mechanical Engineering, Athens, GR-15780, Greece

Correspondence to: Eleni Drakaki (eldrakaki@noa.gr)

Abstract. Dust particles larger than 20 μm in diameter have been regularly observed to remain airborne during long-range transport. In this work, we modify the parameterization of the mineral dust cycle in the GOCART-AFWA dust scheme of WRFV4.2.1, to include also such coarse and giant particles, and we further discuss the underlying misrepresented physical mechanisms which hamper the model in reproducing adequately the transport of the coarse and giant mineral particles. The initial particle size distribution is constrained by observations over desert dust sources. Furthermore, the Stokes' drag coefficient has been updated to account realistic dust particles sizes ($\text{Re} < 10^5$). The new code was applied to simulate dust transport over Cape Verde in August 2015 (AER-D campaign). Model results are evaluated against airborne dust measurements and the CALIPSO-LIVAS pure dust product. The results show that the modelled lifetimes of the coarser particles are shorter than those observed. Several sensitivity runs are performed by reducing artificially the particles' settling velocities in order to compensate underrepresented mechanisms, such as the non-spherical aerodynamics, in the relevant parameterization schemes. Our simulations reveal that particles with diameters of 5.5-17 μm and 40-100 μm are better represented under the assumption of a 80% reduction in the settling velocity (UR80) while particles with sizes ranging between 17 μm and 40 μm are better represented in a 60% reduction in settling velocity (UR60) scenario. The overall statistical analysis indicates that the best agreement with airborne in-situ measurements downwind (Cape Verde) is achieved with a 40% reduction in settling velocity (UR40). Moreover, the UR80 experiment improves the representation of the vertical structure of the dust layers as those are captured by the CALIPSO-LIVAS vertically-resolved pure dust observations. The current study highlights

29 the necessity of upgrading the existing model parameterization schemes of the dust life-cycle components towards improving
30 the assessment of the dust-related impacts within the Earth-Atmosphere system.

31 **1 Introduction**

32 Dust is the most prominent contributor to the global aerosol burden, in terms of dry mass, and it ranks second in
33 aerosol emissions (Gliß et al., 2021; Huneus et al., 2011; Textor et al., 2006). The major sources of dust are situated across
34 the "dust belt" (Prospero et al., 2002) stretching in the Northern Hemisphere hosting deserts and erodible soils (e.g., Goudie
35 and Middleton, 2006), that are prone to windblown dust. Most of the global dust budget comes from the Sahara Desert,
36 followed by deserts in the Middle East and Asia. (Ginoux et al., 2012; Huneus et al., 2011; Kok et al., 2021; Li and Osada,
37 2007). Spatially more limited desert regions in the Southern Hemisphere emit lower amounts of mineral particulate matter
38 (Ginoux et al., 2012; Huneus et al., 2011; Kok et al., 2021; Li and Osada, 2007), and less than 5% comes from high-latitude
39 sources (Bullard et al., 2016).

40 Dust particles act as ice nuclei (IN) on cold cloud processes (Marinou et al., 2019; Solomos et al., 2011) and when
41 mixed or coated with hygroscopic material, they can affect warm cloud processes (Twohy et al., 2009) and serve as cloud
42 condensation nuclei (CCN). Dust particles rich in key micronutrients such as iron (Fe) and phosphorus (P) affect
43 biogeochemical processes in marine and terrestrial ecosystems (Jickells et al., 2005; Okin et al., 2004; Stockdale et al., 2016;
44 Tagliabue et al., 2017) and disrupt the carbon cycle (Jickells et al., 2014) after their wet and dry deposition. Severe dust
45 episodes can affect aviation and telecommunications (Harb et al., 2013; Weinzierl et al., 2012; Nickovic et al., 2021), human
46 health (e.g., Du et al., 2016; Giannadaki et al., 2014) and solar energy production (Kosmopoulos et al., 2018).

47 Apart from the dust load intensity, the size of the suspended mineral particles plays a determinant role on the related
48 impacts on weather and climate, among others. Larger dust particles act more efficiently as CCN (Petters and Kreidenweis,
49 2013) and IN (Diehl et al., 2014) altering cloud microphysical processes and subsequently the hydrological cycle. Recent
50 studies suggest that coarser dust aerosols are more effective absorbers of the incoming solar radiation, enhancing atmospheric
51 warming (Mahowald et al., 2014; Ryder et al., 2019). Therefore, it is imperative to represent realistically the dust particle size
52 distribution (PSD) facilitating a thorough investigation on the dust transport processes and the dust-induced impacts.

53 Airborne dust particles has been observed to sizes up to 300 μm , whereas even larger particles with diameters up to
54 450 μm have been recorded from in situ deposition measurements acquired at buoys mounted across the Tropical Atlantic
55 Ocean (van der Does et al., 2018). Dust particles are usually divided into three different modes (fine, coarse and giant) without
56 strictly defined bounds of their sizes (Goudie, 2014; Knippertz and Stuut, 2014). According to Ryder et al. (2019), the fine
57 mode represents dust particles with $D \leq 2 \mu\text{m}$, the coarse mode those with diameters between 2 μm and 20 μm , and the giant
58 mode particles with $D \geq 20 \mu\text{m}$. A recent study (Ryder et al., in preparation) suggests that the above modes can be further
59 descritized into four categories, namely fine ($D < 2.5 \mu\text{m}$), coarse (2.5-10 μm), super-coarse (10-62.5 μm), and giant ($D > 62.5$
60 μm).

61 The existence of dust particles larger than 20 μm in diameter was already demonstrated in the 1970s based on
62 measurements in the Caribbean (Prospero et al., 1970). Nevertheless, these sizes were neglected in atmospheric dust models
63 since giant particles were assumed to be rare. This assumption has been disproved in recent decades by a large number of
64 airborne campaigns equipped with state-of-the-art in situ and remote sensing instruments. Specifically, in the framework of
65 the SAMUM1 (Weinzierl et al., 2009) and SAMUM2 (Liu et al., 2018) experimental campaigns it has been justified that above
66 sources dust aerosols up to 40 μm in diameter were recorded in 20% of the identified dust layers, while over Cape Verde
67 mineral particles up to 30 μm in diameter were measured (Weinzierl et al., 2011). This reduction of dust particle sizes, along
68 the transport pathway, is attributed to the gravitational settling. Similar findings were reported in the FENNEC campaign
69 (Ryder et al., 2013b) with mean effective particle diameters ranges of 22 to 28 μm and 15 to 18 μm for fresh and aged dust,
70 respectively. During the AER-D campaign, in the Saharan outflow zone near Cape Verde and the Canary Islands, mineral
71 particles with diameters larger than 20 μm were systematically recorded, while in 36% of the studied cases, particles with
72 diameters larger than 40 μm recorded (Ryder et al., 2018). Dust particles with diameters of 10 to 30 μm were detected during
73 the SALTRACE campaign in Barbados (Weinzierl et al., 2017), revealing that they were suspended far away from their sources
74 at about 2000 km more than what would be expected from the Stokes' theory (Weinzierl et al., 2017). Atmospheric dust models
75 are the optimal tool to simulate the components of the dust cycle and therefore to study the dust-related effects. However, the
76 state-of-the-art atmospheric dust models are characterized by inherent limitations in accounting for realistic emission and
77 transport dust size distributions (Huang et al., 2020; Kok, 2010; Mahowald et al., 2014). To overcome these model drawbacks,
78 it is needed to extend the PSD towards the giant particles size spectrum in order to shed light on the processes that sustain
79 larger dust aerosols in the atmosphere for longer periods than expected.

80 Ginoux, (2003) modeled dust aerosols up to 70 μm in diameter using the Global Ozone Chemistry Aerosol Radiation
81 and Transport (GOCART) model and examined the effects of non-sphericity assuming randomly oriented ellipsoidal particles.
82 His results showed that the reduction of the settling velocity results in a better agreement with observations when the aspect
83 ratio is equal or greater than 5. The new modeled particle size distributions (PSDs) were in generally better agreement with
84 the AERONET observations, although the PSDs were significantly underestimated for diameters near 10 μm . The aspect ratio
85 of 5 results in a reduction in settling velocity of about 45% for particles with sphere volume-equivalent diameters near 10 μm
86 and 60% for particles with sphere-volume-equivalent diameters near 30 μm . Maring et al. (2003) applied a simple empirical
87 model and suggested that an upward velocity of 0.0033 ms^{-1} (0.33 cm s^{-1}) is required to accurately predict PSD changes during
88 transport. Although their comparisons were limited to sizes up to 25 μm , they pointed out that unknown or not well-known
89 processes counteract gravity settling. Possible mechanisms which can interpret the aforementioned findings are (i) vertical
90 mixing within the Saharan air layer during the day (Gasteiger et al., 2017), (ii) the lower settling velocities of non-spherical
91 dust particles (Huang et al., 2020; Mallios et al., 2022), (iii) the underrepresented meteorological conditions (O'Sullivan et al.,
92 2020), (iv) the unresolved turbulence (Gu et al., 2021), (v) the electrification of dust (Daskalopoulou et al., 2021; Mallios et
93 al., 2021a; Mallios et al., 2022; Joseph R. Toth III et al., 2020; Renard et al., 2018; Nicoll et al., 2011) and (vi) the numerical
94 errors that perturb the mass balance (Ginoux, 2003).

95 In this work, we demonstrate for the first time a method for incorporating coarse and giant desert dust particles ($D >$
96 $20 \mu\text{m}$, following the definition of the dust modes proposed in Ryder et. al, (2019), into the Advanced Research Weather
97 version of the Weather Research and Forecasting (WRF-ARW) model in conjunction with the GOCART (Ginoux, 2003)
98 aerosol model and the Air Force Weather Agency (AFWA) dust emission scheme (LeGrand et al., 2019) (WRF-GOCART-
99 AFWA model). After pinpointing that the model quickly deposits coarse and giant dust particles, we investigate the reasons
100 behind those findings: We use sophisticated in situ PSD measurements to initialize the model over the sources and to evaluate
101 the simulated PSD over the receptor areas. We also use pure-dust spaceborne retrievals to assess the model performance in
102 terms of reproducing the vertical structure of the dust layers. In addition, we perform a series of sensitivity tests by reducing
103 the settling velocity of mineral particles in the model and we investigate the concomitant effects on dust fields. The article is
104 organized as follows: In Sect. 2, we describe the methodology in terms of the changes we made to the code of WRF-GOCART-
105 AFWA, the setup of the model and the experiments performed, and the observational data we used for model validation. The
106 results of our work are presented in Sect. 3, Sect. 4 contains the discussion and Sect.5 the summary and the conclusions of this
107 work.

108 **2 Model and Data**

109 **2.1. WRF-GOCART-AFWA model**

110 In our numerical experiments to study the transport of coarse and giant dust aerosols, we use the WRF-ARWv4.2.1
111 model coupled with the GOCART aerosol model and the AFWA dust emission scheme (LeGrand et al., 2019). The current
112 version of the WRF-GOCART-AFWA model accounts for giant dust particles in the calculated dust emission fluxes (up to
113 $125 \mu\text{m}$) and assumes that the transported dust particles are up to $20 \mu\text{m}$ in diameter. To extend the transport PSD to coarser
114 and giant mineral particles, we implemented several developments in the standard WRF-GOCART-AFWA model, which are
115 discussed in Sect. 2.1.1 and 2.1.2. Figure 1 shows a sketch of the workflow: the first three steps refer to the implemented
116 modifications in the standard WRF-GOCART-AFWA code: In **step 1**, we establish the definition of a prescribed PSD for the
117 emitted dust particles at the source based on in situ reference measurements, and we distribute the total emitted dust
118 accordingly; in **step 2**, we define five size ranges (five model size bins) for the transported PSD covering dust particle sizes
119 (in diameter) spanning from $0.2 \mu\text{m}$ to $100 \mu\text{m}$ (Sect. 2.1.1); in **step 3**, we implement an updated drag coefficient that applies
120 to the sizes of the entire range of Aeolian dust PSD (Sect. 2.1.2). These code upgrades are integrated into the new WRF-L
121 model. Table 1 shows the properties of the size bins in the standard WRF-GOCART-AFWA code and the size classes defined
122 in the new WRF-L code. At **step 4** we perform model experiments and validate the model results using different model
123 configurations against observations (Sect. 2.2), as described in detail in Sect. 3.

124 **2.1.1 Dust size distribution**

125 In observational studies of non-spherical particles, it is customary to describe their size in terms of spherical volume
 126 equivalent diameter. Here, to describe particles' sizes distributed within the five size bins of the WRF-L model, we use the
 127 sphere-volume-equivalent effective diameter (D_{eff}), which is more relevant to the optical properties of the particles (Hansen
 128 and Travis, 1974). In this way, we simplify the comparison between the model calculations and the observations of the optical
 129 properties of the particles (e.g., dust optical depth). The D_{eff} in (μm) of each size bin is calculated as shown in Eq. 1, and is
 130 provided in Table 1.

131

$$132 \quad D_{eff} = \frac{\int_{D_{lo,k}}^{D_{u,k}} D^3 \cdot \frac{dN}{dD} \cdot dD}{\int_{D_{lo,k}}^{D_{u,k}} D^2 \cdot \frac{dN}{dD} \cdot dD}, \quad (1)$$

133

134 Where D is the particle diameter in (m) and $\frac{dN}{dD}$ is the particle number size distribution in number of particles per m^3 . The
 135 parameters at each size bin k are listed in Table 1. Henceforward, references about the size of the particle correspond to particle
 136 volume equivalent effective diameter, unless mentioned otherwise.

137 In the default GOCART-AFWA dust emission scheme of WRF, the total emitted vertical dust flux is estimated at
 138 each grid point prone to dust emission, when favorable conditions are met. The dust flux is then distributed over five transport
 139 size bins, based on the fragmentation theory of Kok, (2011), bounded to diameters up to $20 \mu\text{m}$. Since our goal is to consider
 140 larger dust particles than those commonly used in the current atmospheric dust models, we redefine the five transport model
 141 bins including particles with diameters up to $100 \mu\text{m}$ (Table 1). We rely on prescribed PSD for the emitted dust particles at the
 142 source based on the airborne in situ measurements acquired during the FENNEC campaign of 2011 (Ryder et al., 2013a). More
 143 specifically, for the freshly uplifted dust we use the mean PSD at the lowest available height (i.e., 1km), obtained by averaging
 144 profile measurements above the Sahara (Mauritania and Mali), hereafter called the "observed FENNEC-PSD", which is shown
 145 in Fig. 2(a) with red squares. Figure 2a shows also the "fitted FENNEC-PSD" (solid red line), which is the fit of the "observed
 146 FENNEC-PSD", using five lognormal modes (Table 4). In Sect. 2.2.1 more information is provided on the derivation of the
 147 mean "observed FENNEC-PSD", including also the description of the FENNEC 2011 campaign, the in-situ instrumentation
 148 used and the processing of the acquired data. Based on the FENNEC-PSD we calculate the mass fraction ($k_{factors}$) distributed
 149 among the redefined transport model size bins in Eq. 2. The weighting factors $k_{factors}$ are shown in Fig.2(b).

150

$$151 \quad k_{factors} = \frac{\int_{D_{lo,k}}^{D_{u,k}} \frac{dV}{d \ln D} \cdot dD}{\int_{D_{lo,k_{min}}}^{D_{u,k_{max}}} \frac{dV}{d \ln D} \cdot dD}, \quad (2)$$

152

153 Where D is the particle diameter, $\frac{dV}{dlnD}$ is the volume size distribution in $\mu\text{m}^3\text{cm}^{-3}$, $D_{l0,k}$ and $D_{u,k}$ are the margins of each size
 154 bin k in μm .

155 2.1.2 Updated gravitational scheme

156 In the GOCART-AFWA dust scheme of WRF, the forces acting on a dust particle moving along the vertical direction
 157 are the gravitational force F_g and the aerodynamic drag force F_{drag} , which are mathematically expressed in Eq.3 and Eq.4,
 158 respectively.

$$159 F_g = \rho_p \cdot V_p \cdot g, \quad (3)$$

$$160 F_{drag} = \frac{1}{2} \cdot \frac{C_D}{C_{cun}} \cdot A_p \cdot \rho_{air} \cdot u_{term}^2, \quad (4)$$

162
 163 Where ρ_p stands for particle density in kgm^{-3} , g corresponds to the gravitational acceleration in ms^{-2} , $V_p = \frac{1}{6} \cdot \pi \cdot D_{eff}^3$ is the
 164 particle volume in m^3 and $A_p = \frac{\pi}{4} \cdot D_{eff}^2$, is the particle's projected area normal to the flow in m^2 , ρ_{air} is the air density in
 165 kgm^{-3} . and D_{eff} represents the particles' diameter in m for each model size bin (assuming spherical particles, as defined in
 166 Sect. 2.1.1). C_D is the aerodynamic drag coefficient (unit less) and C_{cun} is the slip correction to account for slip boundary
 167 conditions (Davies, 1945) and it is expressed as a function of the air mean free path (λ , in meters) (Eq. 5):

$$168 C_{cun} = C_{cun}(\lambda) = 1.0 + \frac{2 \cdot \lambda}{D_{eff}} \left[1.257 + 0.4 \cdot e^{-\frac{1.1 \cdot D_{eff}}{2 \cdot \lambda}} \right], \quad (5)$$

169
 170
 171 The constant velocity that a particle builds up falling vertically within the Earth's atmosphere, is defined as the terminal settling
 172 velocity u_{term} , and it can be estimated by solving the 1-D equation of motion at the steady state limit, where net force is
 173 assumed to be equal to zero:

$$174 \rho_p \cdot V_p \cdot g = \frac{1}{2} \cdot \frac{C_D}{C_{cun}} \cdot A_p \cdot \rho_{air} \cdot u_{term}^2, \quad (6)$$

175
 176
 177 In the default GOCART-AFWA dust scheme the drag coefficient is given by Stokes' Law and is defined as:

$$178 C_D = \frac{12}{Re}, \quad (7)$$

179 Where Re is the Reynold's number (unit less) given by the following equation as a function of the particle volume equivalent
 180 effective diameter D_{eff} :

182

$$Re = \frac{\rho_{air} \cdot u_{term} \cdot D_{eff}}{2 \cdot \mu}, \quad (8)$$

184

185 Where μ is the air dynamic viscosity in $\frac{kg}{m \cdot s}$ defined as a function of air temperature T in K by the following equation (Hilsenrath,
186 1955; United States Committee on Extension to the Standard Atmosphere., 1976):

187

$$\mu = \frac{\beta \cdot T^{\frac{3}{2}}}{T + S}, \quad (9)$$

189

190 where S is the Sutherland constant which equal to $110.4 K$ and β is a constant which equals to $1.458 \cdot 10^{-6} kg \cdot m^{-1} \cdot s^{-1} \cdot$
191 $K^{-1/2}$.

192 and the air mean free path is expressed as:

$$\lambda = \frac{1.1 \cdot 10^{-3} \cdot \sqrt{T}}{P} \quad (10)$$

194 Where T is the air temperature in K and P the air pressure in hPa .

195

196 The slip-corrected drag coefficient of the Stokes' Law ($\frac{12}{Re \cdot C_{cun}}$) is valid only for $Re \ll 1$, thus it is not representative
197 for particles with D_{eff} larger than $\sim 10 \mu m$. Therefore, an adaptation of the drag coefficient is needed in order to be valid for
198 higher Re values (i.e., $0 < Re < 16$), since in our work dust particles with diameters larger than $20 \mu m$ are considered. To realize,
199 we use the drag coefficient C'_D (Eq. 11), proposed by Clift and Gauvin, (1971):

200

$$C'_D = \frac{12}{Re} \cdot (1 + 0.2415 \cdot Re^{0.687}) + \frac{0.42}{1 + \frac{19019}{Re^{1.16}}}, \text{ for } Re < 10^5 \quad (11)$$

202

203 Mallios et al., (2020) used the same C'_D as a reference for the development of a drag coefficient for prolate ellipsoids, as more
204 suitable for $Re < 10^5$. The departures between the drag coefficients given by Stokes and Clift and Gauvin (1971) become
205 more evident for increasing particles' sizes. More specifically, the drag coefficient given by Clift and Gauvin (1971) can be
206 up to 2 times higher than those of the Stokes' Law for coarse and giant particles (Fig. S1).

207

208 In the default WRF code the slip correction is applied unconditionally for all the Re values, probably without affecting
209 the solution significantly due to the small particle sizes ($D_{eff} < 20 \mu m$). However, in our work a condition is required for
210 applying the slip correction only in the Stokes' regime (e.g. $Re < 0.1$, Mallios et. al, 2020). Hence, we apply the bisection
method to calculate the terminal velocity for each model size bin using the revised drag coefficient and, at first, ignoring the

211 slip correction. When the solution lies in the Stokes' regime (e.g. $Re < 0.1$), we recalculate the settling velocity using the
 212 corrected drag coefficient $C'_{D,slip} = \frac{C'_D}{C'_{cun}}$, where $C'_{cun} = C_{cun}(\lambda')$ with λ' the mean free path obtained by (Jennings, 1988):

213

$$214 \quad \lambda' = \sqrt{\frac{\pi}{8} \cdot \frac{\mu}{\sqrt{P\rho_{air}}}}, \quad (12)$$

215 **2.1.3 Model experiments**

216 Using the WRF-L code, we first run the CONTROL experiment. Our simulation period coincides with the AER-D
 217 experimental campaign (29/7 - 25/8/2015) for a domain bounded between the 1.42°N and 39.99°N parallels and stretching
 218 between the 30.87°W and 46.87°E meridians (Fig. 3). The simulation area encompasses the major Saharan also including the
 219 downwind areas in the eastern Tropical Atlantic. We use an equal-distance grid with a spatial grid spacing of 15 km x 15 km
 220 consisting of 550×300 points whereas in vertical, 70 vertical sigma pressure levels up to 50 hPa are utilized (defined by the
 221 model). The simulation period consists of nine 84-hour forecast runs, which are initialized at 12 UTC, using the 6-hour Global
 222 Forecast System Final Analysis (GFS - FNL) reanalysis product, available at a $0.25^\circ \times 0.25^\circ$ spatial grid spacing. The sea surface
 223 temperatures, acquired by the NCEP daily global SST analysis (RTG_SST_HR), are updated every six hours along with the
 224 lateral boundary conditions. Topography is interpolated from the 30-sec Global Multi-resolution Terrain Elevation Data 2010
 225 (GMTED2010, Danielson and Gesch, (2011)). Land use is defined based on the Moderate-resolution Imaging
 226 Spectroradiometer (MODIS) observational data, modified by the University of Boston (Gilliam and Pleim, 2010). From each
 227 84-hours cycle, the first 12 hours are discarded due to model spin up. Likewise, the first week of the simulation served as a
 228 spin-up run for the accumulation of the background dust loading and it is excluded from the analysis. The simulation runs are
 229 performed in a dust-only mode, neglecting the radiative feedback from aerosols. We scale the dust source strength, by tuning
 230 the empirical proportionality constant in the horizontal saltation flux equation (in eq. 10 in LeGrand et al., (2019)) in order to
 231 obtain the best match between the modeled DOD and the AERONET AOD (RMSE=0.34, bias=-0.07) acquired at 8 desert
 232 stations: Banizoumbou, Dakar, El_Farafra, Medenine- IRA, Oujda, Tizi_Ouzou, Tunis_Carthage, Ben_Salem). Note that we
 233 take into account only AERONET records when AODs are higher than 0.2 (Version 3.0, Level 1.5, Giles et al., 2019; Sinyuk
 234 et al., 2020) and the Angstrom exponent is lower than 0.75. The tuning constant is equal to 3 and is applied throughout the
 235 model domain. The complete configuration options for the run are listed in Table 2. The resolution applied in this study (15km
 236 grid spacing) is adequate for the scale of phenomena we want to study, improves the representation of topography and increases
 237 the accuracy of the reproduced weather and dust fields compare to coarser resolution such as used in global datasets (e.g. 0.5
 238 deg GFS) (Cowie et al., 2015; Basart et al., 2016; Roberts et al., 2017; Solomos et al., 2018). WRF-Chem solver uses a 5th-
 239 order horizontal advection scheme and a 3-rd order vertical advection scheme to solve the scalar conservation equation, along
 240 with the 3-rd order Runge-Kutta time integration scheme (Grell et al., 2005). The use of such high-order advective schemes
 241 eliminate the numerical errors of diffusion in the code. We should note though that in the deposition parameterization of

242 GOCART-AFWA dust scheme the vertical advection of the losses due to the gravitational settling is solved by a first order
 243 explicit scheme, which is notoriously too diffusive (Versteeg and Malalasekera, 2007) and thus it can possibly induce
 244 numerical errors in the mass conservation (Ginoux, 2003). A series of additional sensitivity runs has been performed aiming
 245 to resemble possible mechanisms (misrepresented or even absent in the model) counteracting gravitational settling towards
 246 reducing the differences between the CONTROL run calculations and the in-situ observations (shown in Sect. 3.4). To be more
 247 specific, we gradually reduced (with an incremental step of 20%) the settling velocity by up to 80%, with the corresponding
 248 runs named as URx (x corresponds to the reduction in percentage terms). Under such theoretical conditions, it is expected that
 249 the giant dust particles will be suspended for longer periods and that they will be transported at larger distances than the current
 250 state-of-the-art models simulate, failing to reproduce what is observed in the real world. Based on these sensitivity experiments,
 251 we defined a constant (by percentage) relevant reduction of the particles' settling, which in its absolute value varies with size.
 252 Therefore, it is more similar to the effects that are related to aerodynamic forces due to the non-spherical shape and the
 253 orientation of the suspended dust particles (Ginoux, 2003; Loth, 2008; Zastawny et al., 2012; Shao et al., 2017; Sanjeevi et al.,
 254 2018; Mallios et al., 2020). Finally, the full list of the performed experiments is given in Table 3.

255 **2.1.4 Dust extinction coefficient**

256 For the evaluation of the model mid-visible (550 nm) dust extinction profiles the corresponding products from the
 257 Lidar climatology of Vertical Aerosol Structure for space-based lidar simulation studies (LIVAS) dataset is used as reference.
 258 For the spatiotemporal matching between the modelled and the observed dust extinction, we first project the two datasets onto
 259 a common horizontal grid, by converting the model outputs from their native horizontal grid spacing (15 km x 15 km) to the
 260 structured 1°x1° equal lat-lon grid of LIVAS. The model extinction coefficient for each size bin k ($EC_{550,k,n,l}$) is then calculated
 261 at each grid cell n and within each model level l , as shown in Eq.13.

$$263 \quad EC_{550,k,l,n} = \sum_1^k \frac{3}{2\rho_k D_{eff,k}} M_{n,k,l} Q_{ext550,k}, \quad (13)$$

264
 265 where $M_{n,k,l}$, ρ_k , $D_{eff,k}$ and $Q_{ext550,k}$ are the grid cell dust mass concentration in g/m^3 , the particle density in g/m^3 , the effective
 266 diameter in m, and the extinction efficiency factor at 550 nm, of size bin k .

267 $Q_{ext550,k}$ is calculated using the Mie scattering code (Mie, 1908), considering spherical dust particles, and a refractive index
 268 of $1.55 + i0.005$, which is representative of dust (e.g. Dubovik et al., 2002). Although the extinction coefficient values for
 269 spherical particles may be different from the extinction coefficient values of the dust particles, which have irregular shapes, to
 270 our knowledge there is no data available for the extinction coefficient of the latter. The extinction coefficient values of
 271 spheroidal shapes, commonly used as a proxy of the dust shapes, are not substantially different compared to the spherical
 272 particles (Tsekeri et al., 2022), at least when considering the aspect ratios measured for dust particles in Sahara (Kandler et al.,
 273 2009). For simplifying the computations, we assume that the particles in each size bin have the same size (i.e. $D_{eff,k}$), and thus

274 the same $Q_{ext550,k}$. In vertical, the fine resolution LIVAS dust extinction coefficient is rescaled (averaging) to match the model
275 layers vertical margins. In the time dimension, the model outputs at the closest lead times to the satellite overpass are selected.

276 **2.2 Observational datasets**

277 **2.2.1 Airborne in situ observations**

278 During the FENNEC field campaign in 2011 (Ryder et al., 2013b, 2013a) and the AER-D field campaign in 2015
279 (Ryder et al., 2018, 2019), airborne in situ observations were collected with the FAAM BAE research aircraft. In this study
280 we use size distributions from the FENNEC field campaign, acquired during aircraft profiles over the Sahara (Mauritania and
281 Mali), as described in Ryder et al. (2013a). We select size distributions from “freshly uplifted dust” cases, when dust particles
282 are in the atmosphere for less than 12 h. Additionally, from these profiles we use data from the lowest available altitude,
283 centered at 1km, covering altitudes between 0.75 to 1.25km. The derived PSD is depicted in Fig.2(a), hereafter referred to as
284 the “observed FENNEC-PSD”. Error bars in Fig.2(a) indicate the standard deviation of the observed values across the profiles
285 and altitudes we used. The instrumentation for those measurements was the Passive Cavity Aerosol Spectrometer Probe
286 (PCASP, 0.13-3.5 μm), the Cloud Droplet Probe (CDP, 2.9-44.6 μm), using light scattering measurements and assuming a
287 refractive index (RI) of 1.53-0.001i (which is constant with particle size), spherical shape for the particles, and using Mie
288 calculations to convert from optical to geometric diameter, as well as the Cloud Imaging Probe (CIP15, 37.5-300 μm). The
289 instruments and data processing are described in Ryder et al. (2013a). The midpoint size bin diameters do not overlap, though
290 there is some overlap in bin edges between the instruments. A fit on the observations is provided in Figure 2a (the “fitted
291 FENNEC-PSD” with solid red line), which is used in the parameterization of the emitted dust, as described in Section 2.1.1,
292 to modify the GOCART-AFWA dust scheme in WRF.

293 We also use PSD observations during horizontal flight legs at a constant height (referred either as RUNs or flight
294 segments) over the Atlantic Ocean during AER-D. We use measurements taken with PCASP ($D=0.12-3.02 \mu\text{m}$) for fine dust
295 particles. For the coarse and giant mode of dust we used measurements from CDP ($D=3.4-20 \mu\text{m}$, although CDP measurements
296 availability extends up to 95.5 μm as it is explained below) and the two-dimension Stereo probe (2DS, $D=10-100 \mu\text{m}$ -
297 although the instrument measures up to 1280 μm few particles larger than 100 μm were detected). For the light scattering
298 techniques of PCASP and CDP, a RI = 1.53-0.001i is assumed for the conversion of the optical to geometric diameter (as in
299 FENNEC 2011 campaign). CDP observations extend up to the size of 95.5 μm , thus data from CDP and 2DS partly overlap in
300 their size range. Since 2DS observations are more reliable in the overlapping size range, we used the CDP observations for
301 particles with sizes up to 20 μm . Also, 2DS-XY observations are preferred over the 2DS-CC, since they better represent the
302 non-spherical particles. A more detailed description of the in-situ instruments and the corresponding processing of the data
303 acquired during the AER-D campaign is included in Ryder et al., (2018). The error bars represent the total (random and
304 systematic) measurement error due to the counting error, the discretization error, the uncertainties in the sample area and the

305 uncertainties in the bin size due to Mie singularities (Ryder et al., 2018). All PSD measurements are at ambient atmospheric
306 conditions. The locations of the flights of AER-D used in this study are depicted in Fig.3.

307 **2.2.2 LIVAS product**

308 For the validation of the vertical distribution of dust from the model (see Sect. 3.5), we utilize the pure-dust profiles
309 provided by the LIVAS dataset, originally presented in Amiridis et al. (2013; 2015) and updated in Marinou et al. (2017). The
310 LIVAS pure-dust product is a global dataset, covering the period between 06/2006 and 05/2020, and is provided a) on per-
311 granule level with similar resolution to the original Cloud-Aerosol Lidar and Infrared Pathfinder Satellite Observations
312 (CALIPSO) L2 profile products (i.e., 5 km horizontal and 60 m vertical), and b) as a global three-dimensional database of
313 monthly-mean averaged profiles of aerosol properties, on a uniform horizontal grid spacing of $1^\circ \times 1^\circ$. LIVAS was developed
314 applying the dust-separation technique described in Tesche et al., (2009) on the CALIPSO level 2 version 4 products (Winker
315 et al., 2009). The LIVAS pure-dust product has been used to a variety of dust-oriented studies including the investigation of
316 the dust sources and the seasonal transition of the dust transport pathways (Marinou et al., 2017; Proestakis et al., 2018); the
317 evaluation of the performance of atmospheric and dust transport models (e.g. Tsikerdekis et al., 2017; Solomos et al. 2017;
318 Georgoulas et al., 2018; Konsta et al., 2018), the evaluation of new satellite-based products (e.g. Georgoulas et al., 2016;
319 Chimot et al. 2017; Georgoulas et al., 2020; Gkikas et al., 2021), and on dust assimilation experiments (Escribano et al., 2021).
320 Herein, the LIVAS pure-dust extinction product is used for the assessment of the simulated dust vertical patterns. In the
321 geographical region of our study, the uncertainty of the product is estimated to be less than 20% in altitudes up to 6km (Marinou
322 et al. 2017).

323 **3 Results**

324 **3.1 Settling Velocities**

325 Figure 4 shows the altitude profiles of the settling velocities for each size bin from the CONTROL run, averaged over
326 the simulation domain, and the period of interest. Settling velocity increases for larger mineral particles. The terminal
327 velocities for particles within bin 5 are two orders of magnitude higher than those in bin 2 and bin 3, and one order of magnitude
328 with respect to bin 4. An altitude dependency, regulated by the thermodynamic state of the atmosphere, of the terminal
329 velocities is also apparent in Figure 4, showing that they increase with height due to the reduction either of temperature or air
330 density (Eqs. 9 and 13) For the CONTROL run the average settling velocities near the surface are lower by approximately
331 10% than those at 6 km height, and this non-negligible reduction can be critical, particularly for coarser and giant particles
332 where velocities are higher.

333 3.2 Dust above the sources

334 In Fig. 5 we present how the PSD varies with height above an emission point (latitude=24.9° and longitude=9.2°) in
335 Mali, on 11/08/2015 at 14UTC. The model PSDs are only from that grid model box interpolated at 1, 2, and 3 km height and
336 for the particular timestep (11/08/2015 at 14UTC). The red squares correspond to the “observed FENNEC-PSD” sorted into
337 the five bins. The error bars provide the maximum and minimum limits of the “observed FENNEC-PSD”, sorted into the five
338 model size bins, after including the standard deviation of “observed FENNEC-PSD”. The “observed FENNEC-PSD” (see
339 Section 2.2.1) has been derived from several flights above dust sources, thus it is representative of the PSDs above Sahara
340 sources and it used here as reference. The black squares depict the “fitted FENNEC-PSD” sorted into five bins, used in the
341 model parameterization to calculate the emitted dust mass of the corresponding five model transport bins. The difference
342 between the “fitted FENNEC-PSD” and the “fitted FENNEC-PSD” occurs due to the fitting process. The modelled volume
343 concentration is reduced with height by an order of magnitude between 2 and 3 km for particles with diameters 17-40 μm (bin
344 4). At 3km the simulated concentrations of particles in bin 4 and bin 5 are very low compared to the measurements in Fig. S2a
345 of Ryder et al., (2013a) which indicate the removal of giant particles above 4 km (Ryder et al., 2013a, Figure S2a). Although
346 a direct comparison between the modelled and the observed PSD for this particular emission point is not feasible, since the
347 FENNEC campaign took place on different dates than the AER-D and there are no available measurements above dust sources
348 for the period we performed our simulations, we note a modification of the PSD shape, both for model and observations at
349 1km. It is evident that the model overestimates the PSD for bins 1-3 while the opposite is found in the size spectrum of the
350 super-coarse (bin4) and giant (bin5) dust particles. Therefore, a model weakness is revealed at the very early phase of the dust
351 transport. Those differences can be attributed to an overestimation of their loss during uplift from the surface to 1 km, or to
352 higher updrafts that remain unresolved in our numerical experiment. Another possible source of this underestimation could be
353 the utilization of a not well-defined PSD shape constraining the distribution of emitted dust mass to the model transport size
354 bins. The use of a PSD with a higher contribution of coarse and giant dust particles could possibly improve the representation
355 of the coarse and giant particles aloft (Fig. S2 and S3) and can be assessed in future studies. Additionally, comparing the
356 “observed FENNEC-PSD” with the modelled PSD of the scenario with the maximum relative reduction of the settling
357 velocities (UR80) in Fig. 5, we find a significant increase of the modelled volume concentrations, reducing the differences
358 seen in volume concentrations in bin4 and bin5 without the reduction of the settling velocity, although the underestimation in
359 bin 5 is still evident.

360 3.3 Mean dust load

361 In Fig. 6, the spatial patterns of the columnar dust concentrations are depicted, averaged over the period of 5/8/15-
362 25/8/15, for the total mass as well as for each one of the five size bins simulated with the CONTROL run. Among the first
363 three bins, there are evident many similarities of the dust load spatial features, with maximum values in the Western Sahara
364 whereas the dust advection pathways towards the Atlantic Ocean are clearly seen. In terms of intensity, the mass increases

365 from bin1 to bin 3 (5.5 – 17 μm), yielding the maximum values throughout the size ranges. Dust particles with diameters
366 between 17 μm and 40 μm (bin 4) are found mainly over land, and are subjected to short-range transport westwards (i.e., off
367 the Moroccan coast). Giant particles (bin 5) are found at very low concentrations ($< 0.5 \text{ gr m}^{-2}$), at isolated areas over/near dust
368 sources, since the strong impact of gravitational settling prohibits their accumulation and transport.

369 **3.4 Dust size distribution**

370 Figure 7 illustrates the simulated PSDs, from each experiment (i.e., CONTROL and URx), along with those acquired
371 by the airborne in situ measurements at different segments and altitudes of the flight b928 in the surrounding area of Cape
372 Verde (downwind region). For the other AER-D flights (i.e., b920, b924, b932 and b934) similar findings are drawn and for
373 brevity reasons are omitted here and are included in the supplementary material (Fig.S4). All AER-D measurements
374 demonstrate the impacts of the processes that are associated with dust transport. The red squares represent the observations
375 and the error bars represent the total (random and systematic) measurement error (see Sect 2.2.1). The modelled PSDs are
376 collocated in space and time with the measurements of each flight segment. For each flight segment, we extract the modeled
377 PSD by interpolating the dust field to the specific altitude of the flight RUN. Additionally, we average the dust field of the
378 nearest grid cell to each coordinate pair along the flight segment track, and the eight neighbouring grid cells of the same
379 altitude. The coordinates of the flight leg track are depicted with orange dots and the collocated grid points used for deriving
380 the modelled PSD (at the specific height of each flight leg) with blue dots. In the time dimension, we average the two hourly
381 model outputs that contain the times of the measurement. In case that the time of measurement coincides with the exact hourly
382 output, the model output on that hour along with the outputs prior and after that are averaged. The error bars in the model PSDs
383 indicate the standard deviation of the collocated grid points averaging in space and time.

384 Based on our findings, for the CONTROL run, the model performs considerably well particularly near the surface
385 and above 4 km, reproducing the volume concentration of the particles residing within bins 1 and 2. Underestimations are
386 found for the third bin with the simulated volume concentration falling however within the measurement uncertainties
387 envelope. As expected, for bins 4 and 5, the model is not capable of reproducing the observed PSD at distant areas since quite
388 significant underestimations have been already notified above sources (see Fig. 5a). The reduction of the settling velocity (i.e.,
389 URx runs, see Table 3) has negligible impact on the level of agreement between model and observations for bins 1 and 2,
390 moderate for bin3 while is determinant for the super-coarse (bin 4) and giant (bin 5) dust particles. Nevertheless, for achieving
391 the best model-observations matching, the necessary reduction (expressed in percentage) on the settling velocity is not constant
392 among the defined transport bins. Focusing on bins 4, the UR60 run (i.e., reduction of the settling velocity by 60%) outperforms
393 the other numerical experiments and focusing on bin 5 the UR80 run.

394 The overall comparison of the observed and modelled average PSDs is presented in Fig 8. We are considering all the
395 in situ airborne measurements and the WRF-L numerical outputs satisfying the defined spatiotemporal collocation criteria.
396 Error bars indicate the corresponding standard deviation. Figure 8a shows that the best model performance is found for the
397 UR80 experiments resembling satisfactory the bin 4 and bin 3/5 concentrations, respectively. These “artificial” reductions

398 translate to settling velocities equal ~ 0.066 for bin 3 ($D=5.5-17 \mu\text{m}$), ~ 0.32 m/s for bin 4 ($D=17-40 \mu\text{m}$) and ~ 1.88 m/s for bin
399 5 ($D=40-100 \mu\text{m}$). it is also reminded that for the same experiment it has been achieved the best agreement against the
400 FENNEC-PSD above dust sources (see Fig. 5 and the relevant discussion).

401 An alternative comparison between observations and model volume concentrations, for the selected AER-D samples
402 (each flight segment is denoted with different marker), has been performed and the obtained results, at each flight altitude, are
403 depicted in Figure 8b. More specifically, we calculate for each model experiment (denoted with different colour), the relative
404 differences (expressed in percentage) of the total dust volume concentration with respect to the in-situ measurements. In
405 addition, the corresponding differences (in percentage terms) that are representative for the altitudes spanning from near-
406 surface up to ~ 4.2 km are denoted with the vertical coloured dashed thick lines (WRF-L experiments). Those differences are
407 derived by averaging the relative differences of each flight segment. Overall, the model tends to underestimate the total dust
408 volume concentration (relative differences up to 100% in absolute terms) even though occasionally positive departures are
409 found, as indicated by the spread of the individual biases around zero. Nevertheless, the main finding from this analysis is that
410 the model-observation deviations reduce when the settling velocity reduces too (i.e., URx runs). Among the WRF-L
411 experiments, the minimum biases ($\sim 5\%$) are obtained for the UR40 scenario (i.e. the vertical orange dashed line resides close
412 to zero). Through the inspection of the vertically resolved “behavior” of the individual runs, it is revealed that in some cases
413 the model-observation biases can be minimized for the UR60 and UR80 runs and this “variability” highlights the complexity
414 of the underlying mechanisms governing the suspension of airborne dust.

415 **3.5 Dust vertical distribution**

416 Figure 9(a) shows the profile of the mean extinction coefficient at 532 nm, provided by the LIVAS pure-dust product
417 (black line), and the profile of the mean extinction coefficients at 550 nm, provided by the CONTROL, UR20, UR40, UR60,
418 and UR80 experiments. The orange area indicates the standard deviation of the LIVAS profiles. Figure 9(b) depicts the mean
419 absolute model bias with respect to LIVAS profiles for the different simulations and the vertical dashed lines show the
420 corresponding bias averaged over different altitudes. The mean LIVAS profile is provided by averaging the night-time profiles
421 over the region between 25.5°W to 12.5°E and 11.5°N to 35.5°N , during 5 to 25 August 2015. This area includes the main
422 dust sources that affected the vicinity of Cape Verde (Ryder et al., 2018) and the region of the dust outflow over the Ocean, as
423 well. The nighttime profiles excel in accuracy over the daytime ones, due to the lower signal-to-noise ratio (SNR) during the
424 night. The model profiles are collocated in space and time with the LIVAS profiles, as described in Sect. 2.1.4 and the model
425 extinction coefficient is provided with the Eq.13.

426 The intercompared profiles are in good agreement, with the simulations falling well-within the variability of the dust
427 observations, although discrepancies are also present, especially close to the dust sources, in the nighttime boundary layer
428 (Fig.9(b) – region I), and within the upper free Troposphere (Fig. 9(b) – region III). The assessment of the different model
429 experiments against the ESA-LIVAS pure-dust product is performed in the region between 1.5 km and 6.4 km a.m.s.l. (Fig. 9
430 – region II), to avoid possible biases propagating into the analysis (i.e., complex topography and surface returns-region I, SNR

431 and tenuous aerosol layers – region II). According to the comparison of observations and simulations of the mean extinction
432 coefficient (Fig. 9(a)), the statistical overall analysis reveals that the UR40 experiment demonstrates a better performance
433 compared to LIVAS, reducing the mean bias close to zero. For the same experiment the minimum mean bias with respect to
434 the total volume concentration is achieved (see discussion of Fig.9b in Sect. 3.4). However, the UR80 experiment provides a
435 more constant (positive) bias with height, which suggests a better distribution of the dust mass in the vertical.

436 **4 Discussion**

437 The frequent presence of large desert dust particles ($D > 20 \mu\text{m}$) far from their sources, is well established by numerous
438 observational studies over the last decade (van der Does et al., 2018; Liu et al., 2018; Ryder et al., 2013a, 2013b, 2018, 2019a;
439 Weinzierl et al., 2009, 2011, 2017). However, the processes that result in the particle retainment in the atmosphere, and
440 subsequently their travel at greater distances than predicted, remains unrevealed. In this study we extend the particle size range
441 applied in the transport parameterization of the GOCART-AFWA dust scheme of WRF, to include particles with diameters up
442 to $100 \mu\text{m}$. The evaluation against airborne in situ observations of the size distribution shows that the concentrations of the
443 larger particles are underestimated, both above dust sources and distant areas. This suggests that there are atmospheric
444 processes that are not taken into account in the model simulations. We investigate the effect of reducing the settling velocity
445 of the dust particles due to these unknown processes, and we see that for a reduction of 60% and (especially for) 80%, the
446 simulations of the PSD in Cape Verde are improved with respect to the observations. The reduction of 80% corresponds to a
447 reduction in settling velocity of 0.0066 m/s for particles with D between 5.5 and $17 \mu\text{m}$, which is double than the value reported
448 by Maring et al. (2003) for similar sizes. It should be noted though that Maring et al. (2003) derived this settling velocity using
449 observations that were taken with a five-year difference. Ginoux (2003), has also reported an improvement in model
450 simulations for a reduction in settling velocity of approximately 45% and 60%, for particles with diameters 10 to $30 \mu\text{m}$.
451 Though, the differences in the model resolution, the dust scheme and the drag coefficient in Ginoux (2003) compared to this
452 study, could cause the different values of the required corrections in the settling velocities. The difference with the values
453 suggested herein, can mainly be attributed to the different drag coefficient used in Ginoux (2003), which results in lower
454 settling velocities for the spherical particles. Meng et al. (2022) performed a study, similar to this, where after reducing the
455 settling velocity by 13% for accounting for particles' asphericity based on Huang et al., (2020), performed sensitivity tests
456 reducing the dust particles' density from 2500 kg m^{-3} to 1000 , 500 , 250 and 125 kg m^{-3} . They found that a decrease in the
457 modelled dust aerosol density by 10-20 times its physical value (2500 kg m^{-3}) is needed to improve the comparison between
458 the model and the long-range dust observations of coarse particles. A 10 times reduction in particles' density is almost equal
459 to a 90% reduction in the settling velocity (starting from the Clift and Gauvin (1971) drag coefficients and assuming conditions
460 of U.S. Standard Atmosphere, Fig. S1). It is clear that a huge reduction in the settling velocity in both the Meng et al., (2022)
461 methodology and this work is required, although the physical processes occurring to explain this reduction are not clear.

462 One of the processes proposed in the literature to explain the longer atmospheric lifetimes of large mineral dust
463 particles is the particle asphericity. Ginoux (2003) compared randomly-oriented prolate spheroids and spheres of the same
464 cross section. They showed that spheroids fall slightly slower than their spherical counterparts, with their difference being
465 negligible for spheroids with aspect ratio values less than 5. Huang et al. (2020) compared randomly-oriented ellipsoids and
466 spheres of the same volume. They showed that ellipsoids fall around 20% slower than spheres. Mallios et al. (2020) compared
467 prolate spheroids and spheres of the same maximum dimension, and of the same volume. Moreover, they did not assume
468 randomly-oriented particles, but particles of specific orientation (horizontal and vertical). They showed that the results of the
469 comparison change when the maximum dimension or the volume-equivalent size is used in the comparison. Prolate spheroids,
470 with aspect ratio values in the range of 1.4-2.4, fall slower than spheres of the same maximum dimension, regardless of
471 orientation, with the relative difference between the settling velocities reaching the value of 52%. On the other hand, prolate
472 spheroids, in the same aspect ratio value range, fall faster than spheres of the same volume, regardless of orientation. The
473 comparison with in situ observations of the maximum dimension of particles is not so common, since most of the in-situ
474 measurements do not provide the sizing of the particles in terms of their maximum dimension, with some exceptions, as e.g.
475 the observations shown in van der Does et al. (2016) of individual giant mineral particles (larger than 100 μm in maximum
476 dimension).

477 All the above show that more work is needed for the definite and accurate quantification of the particle asphericity
478 effect on their settling. Nevertheless, there are indications pointing that aspherical particles remain in the atmosphere longer,
479 and that asphericity can be one of the reasons for the differences between the modelling results and the observations.

480 Another process that can influence mineral dust settling has to do with the electrical properties of dust particles. The
481 dust particles are charged in the atmosphere either due to the attachment of atmospheric ions on them (Mallios et al. 2021b)
482 or/and due to collisions, a process known as triboelectric effect (Ette, 1971, Eden and Vonnegut, 1973, Mills, 1977, Jayaratne,
483 1991, Mallios et al., 2022). Moreover, there is a large-scale atmospheric electric field, due to the potential difference between
484 the lower part of the Ionosphere and the Earth's surface (Rycroft et al., 2008). The electric field is modified by ion attachment
485 process (Mallios et al. 2021b) or by the charge separation caused by updrafts (Krauss et al., 2003). Therefore, electrical forces
486 are generated that might influence the particle settling process by balancing the gravity or changing the particle orientation.
487 The quantification of the particles' electrical properties is still an open question

488 Another possible source of error in the gravitational losses simulated by the model as proposed by (Ginoux, 2003) is
489 the numerical diffusion in the advection equation of gravitational settling. Since in the GOCART-AFWA dust scheme of WRF
490 (and WRF-L) a first-order upwind scheme is adapted for the gravitational losses, which is rather diffusive (Versteeg and
491 Malalasekera, 2007), an investigation of the possible improvement on the results by the replacement of the scheme with a less
492 diffusive would be of interest. A possible limitation of this study is the accuracy of the PSD which is used for the distribution
493 on the model transport bins of the emitted fluxes. The simplification in the assumption that the shape of the PSD at 1km above
494 the sources remains unchanged in lower heights near the ground, could possibly introduce errors in the representation of the
495 presence of dust particles aloft.

496 In any case, the proposed scheme presented here, provides a useful tool for the investigation of the physical processes
497 in the transport of coarse and giant particles, along with their impacts on other physical processes in the atmosphere, such as
498 ice nucleation and radiation interactions. The artificial reduction in the settling velocity is not attributed to a known physical
499 mechanism (although results from the past literature reveal some candidates that can give results on the same order of
500 magnitude). Thus, despite the encouraging results, more research is needed towards understanding the physical or numerical
501 processes driving this finding, including the estimation of the impact of non-spherical particles, electricity, the radiation impact
502 on thermodynamics and the disturbance of the mass balance due to the numerical diffusion.

503 **5 Summary and conclusions**

504 In the current state-of-the-art atmospheric dust models, several physical processes governing dust life cycle
505 components are not well represented or they are not included in the relevant parameterization schemes. This drawback, along
506 with the lack of knowledge on the underlying mechanisms, results in the failure of the numerical simulations to reproduce
507 adequately the long-range transport of super-coarse and giant mineral particles, as it has been justified via their evaluation
508 versus sophisticated dust observations. Among the model limitations, well documented in literature, one of the critical is the
509 neglect of mineral particles with diameters larger than 20 μm , under the erroneous assumption that they deposit quickly after
510 their emission.

511 In the current study, we modify the transport particle size distribution in WRF, expanding at size ranges up to 100
512 μm in diameter, by constraining the shape of the modelled PSD with the observed one above dust sources, acquired in the
513 framework of the FENNEC 2011 campaign. A novelty of our work constitutes the upgrade of the drag coefficient, determining
514 the settling velocity of dust particles, for accounting realistic dust particles sizes ($\text{Re} < 10^5$), opposite to what is assumed in the
515 traditional Stokes' theory. After optimally tuning the CONTROL run, we performed a series of sensitivity experiments in
516 which the settling velocity has been reduced, aiming to artificially resemble the real forces acting on particles moving vertically
517 and counteract gravitational settling. Our period of interest spans from 5th to 25th August 2015, when the AER-D campaign
518 took place in the surrounding area of Cape Verde, residing in the core of the "corridor" of the Saharan dust transport along the
519 Tropical Atlantic Ocean. In our experiments, the simulation domain covers most of the Sahara Desert (encompassing the most
520 active dust sources worldwide) and the eastern sector of the Tropical Atlantic Ocean (receiving large amounts of mineral
521 particles from the nearby Saharan dust sources). The dust-related numerical outputs produced by the CONTROL and URx
522 (referring to the reduction of the settling velocity by 20%, 40%, 60% and 80% and it is expressed by the term x) experiments
523 are evaluated against the LIVAS satellite datasets providing pure dust extinction vertical profiles. Nevertheless, special
524 attention is given on the evaluation of the WRF-L PSD against airborne in-situ measurements acquired in the framework of
525 the AER-D campaign.

526 Based on our results, in the CONTROL experiment, the model tends to underestimate the dust volume concentration
527 of coarse and giant dust particles (FENNEC) since the very early stage of dust transport, when the emitted mineral particles

528 are uplifted at 1 km above the sources. Subsequently, the initially obtained model underestimation becomes more pronounced,
529 against those measured in AER-D, particularly for the super-coarse (bin 4, diameters from 17 to 40 μm) and giant (bin 5,
530 diameters from 40 to 100 μm) dust particles, in the vicinity of Cape Verde (i.e., downwind region). Our findings are in line
531 with the already stated underestimation of the presence of coarse and giant dust particles' presence during their long range
532 dust transport. Nevertheless, when we gradually reduce the settling velocity (URx runs) the model performance steadily
533 improves. Overall, among the numerical experiments, the best match of the simulated and the observed PSDs is achieved for
534 the UR80 scenario (i.e., reduction of the settling velocity by 80%), thus highlighting the misrepresentation or the absence of
535 forces, within the model parameterization schemes, acting on dust particles and counteract gravitational settling. Through the
536 case-by-case inspection, it is revealed that the UR60 and UR40 scenarios can also occasionally provide the optimum model-
537 observations agreement thus highlighting the complexity of the real physical processes that regulate dust particles' settling
538 velocity and suspension. From the evaluation of the vertically resolved simulated dust extinction against the corresponding
539 measurements from the LIVAS dataset, it is revealed that for the UR40 run the model-observations are minimized (oscillating
540 around zero) whereas the UR80 run outperforms in reproducing the vertical structure of the dust layers within the Saharan Air
541 Layer. Summarizing, our work demonstrated an innovative approach in order to overcome existing drawbacks of the
542 atmospheric-dust models towards improving the simulations of dust transport along the Tropical Atlantic Ocean. There are
543 several candidate mechanisms, along with inappropriate definition and treatment of mineral particles in the parameterization
544 schemes, hampering models in reproducing adequately the observed dust patterns. Despite our encouraging results, there are
545 many mandatory steps towards upgrading the current state-of-the-art atmospheric dust models in anticipation of an optimum
546 assessment of the multifaceted role of dust aerosols within the Earth-Atmosphere system.

547

548 **Author Contributions:** ED, VA, and AT design the study; SM guided ED on the methodology for the replacement of the drag
549 coefficient. AT provided useful assistance on the treatment of airborne observations. CR provided the data from the airborne
550 in situ measurements and provided useful information about the instrumentation methods. ED developed the code, performed
551 the simulations and analyzed the results. AG and CR consulted ED on the methodology of in situ and WRF datasets. VA, EM
552 and EP provided the LIVAS dataset, lead the collocation methodology and helped on the interpretation of the results. ED
553 plotted the model and observation data (apart from LIVAS). EP treated and plotted LIVAS data; ED wrote the manuscript
554 draft; VA, AT, AG, EP, SM, CS, SS, EM, CR, DB and PK provided critical feedback and reviewed and edited the manuscript.

555

556 **Funding:** This research was supported by the project “PANhellenic infrastructure for Atmospheric Composition and climatE
557 change” (no. MIS 5021516), which is implemented under the action “Reinforcement of the Research and Innovation
558 Infrastructure”, funded by the “Competitiveness, Entrepreneurship and Innovation” Operational Programme (NSRF 2014–
559 2020) and co-financed by Greece and the European Union (European Regional Development Fund). Support was also provided
560 by D-TECT (Grant Agreement 725698) funded by the European Research Council (ERC). ED would like to acknowledge
561 funding by Greece and the Stavros Niarchos Foundation (SNF). CLR was funded by NERC grant reference NE/M018288/1.

562 EM was funded by the European Research Council
563 661 (grant no. 725698, D-TECT) and by a DLR VO-R young investigator group and the Deutscher Akademischer
564 Austauschdienst (grant no. 57370121). AG acknowledges support by the Hellenic Foundation for Research and Innovation (H.
565 F. R. I.) under the “2nd Call for H. F. R. I. Research Projects to support Post-Doctoral Researchers” (project acronym:
566 ATLANTAS, project number: 544).

567
568 **Acknowledgements:** This work was supported by computational time granted from the National Infrastructures for Research
569 and Technology S.A. (GRNET S.A.) in the National HPC facility - A-IS - under project ID pa210502-TRAP-P. We thank the
570 PANhellenic GEophysical observatory of Antikythera (PANGEA) for providing access to the LIVAS data used in this study
571 and their computational center. The National Centers for Environmental Prediction (NCEP) is gratefully acknowledged for the
572 provision of the Global Forecasting System (GFS) operational analyses and the real time global (RTG) sea surface temperature
573 (SST) analyses. We would like to thank the NASA CALIPSO team and NASA/LaRC/ASDC for making the CALIPSO
574 products available, which have been used to build the LIVAS products, and ESA, who funded the LIVAS project (contract no.
575 4000104106/11/NL/FF/fk).

576
577 **Data Availability:** The model outputs and the data used for the analysis are available upon request from Vassilis Amiridis
578 (vamoir@noa.gr) and/or Eleni Drakaki (eldrakaki@noa.gr). The LIVAS dust products are available upon request from Vassilis
579 Amiridis (vamoir@noa.gr), Emmanouil Proestakis (proestakis@noa.gr), and/or Eleni Marinou (elmarinou@noa.gr).

580
581 **Code Availability:** The source code of WRF-L is available upon request from Vassilis Amiridis (vamoir@noa.gr) and/or Eleni
582 Drakaki (eldrakaki@noa.gr).

583 **References**

584 Amiridis, V., Wandinger, U., Marinou, E., Giannakaki, E., Tsekeri, A., Basart, S., Kazadzis, S., Gkikas, A., Taylor, M.,
585 Baldasano, J. and Ansmann, A.: Optimizing CALIPSO Saharan dust retrievals, *Atmos. Chem. Phys.*, 13(23), 12089–12106,
586 doi:10.5194/acp-13-12089-2013, 2013.

587 Amiridis, V., Marinou, E., Tsekeri, A., Wandinger, U., Schwarz, A., Giannakaki, E., Mamouri, R., Kokkalis, P., Biniotoglou,
588 I., Solomos, S., Herekakis, T., Kazadzis, S., Gerasopoulos, E., Proestakis, E., Kottas, M., Balis, D., Papayannis, A., Kontoes,
589 C., Kourtidis, K., Papagiannopoulos, N., Mona, L., Pappalardo, G., Le Rille, O. and Ansmann, A.: LIVAS: a 3-D multi-
590 wavelength aerosol/cloud database based on CALIPSO and EARLINET, *Atmos. Chem. Phys.*, 15(13), 7127–7153,
591 doi:10.5194/acp-15-7127-2015, 2015.

592 Basart, S., Vendrell, L. and Baldasano, J. M.: High-resolution dust modelling over complex terrains in West Asia, *Aeolian*
593 *Res.*, 23, 37–50, doi:10.1016/j.aeolia.2016.09.005, 2016.

594 Bullard, J. E., Baddock, M., Bradwell, T., Crusius, J., Darlington, E., Gaiero, D., Gassó, S., Gisladdottir, G., Hodgkins, R.,
595 McCulloch, R., McKenna-Neuman, C., Mockford, T., Stewart, H. and Thorsteinsson, T.: High-latitude dust in the Earth
596 system, *Rev. Geophys.*, 54(2), 447–485, doi:10.1002/2016RG000518, 2016.

597 Chimot, J., Pepijn Veefkind, J., Vlemmix, T., De Haan, J. F., Amiridis, V., Proestakis, E., Marinou, E. and Levelt, P. F.: An
598 exploratory study on the aerosol height retrieval from OMI measurements of the 477 nm O₂ spectral band using a neural
599 network approach, *Atmos. Meas. Tech.*, 10(3), 783–809, doi:10.5194/amt-10-783-2017, 2017.

600 Cowie, S. M., Knippertz, P. and Marsham, J. H.: A climatology of dust emission events from Northern Africa using long-term
601 surface observations, *Atmos. Chem. Phys.*, 14(16), 8579–8597, doi:10.5194/acp-14-8579-2014, 2014.

602 Clift, R. and Gauvin, W. H.: Motion of entrained particles in gas streams, *Can. J. Chem. Eng.*, 49(4), 439–448,
603 doi:10.1002/cjce.5450490403, 1971.

604 Clift, R., Grace, J. R. and Weber, M. E.: *Bubbles, Drops, and Particles*, Dover Publications. [online] Available from:
605 <https://books.google.gr/books?id=UUrOmD8niUQC>, 2005.

606 Danielson, J. J. and Gesch, D. B.: Global multi-resolution terrain elevation data 2010 (GMTED2010), Open-File Report,
607 <https://doi.org/10.3133/ofr20111073>, 2011.

608 Daskalopoulou, V., Mallios, S. A., Ulanowski, Z., Hloupis, G., Gialitaki, A., Tsikoudi, I., Tassis, K. and Amiridis, V.: The
609 electrical activity of Saharan dust as perceived from surface electric field observations, *Atmos. Chem. Phys.*, 21(2), 927–949,
610 545 doi:10.5194/acp-21-927-2021, 2021.

611 Davies, C. N.: Definitive equations for the fluid resistance of spheres, *Proc. Phys. Soc.*, 57(4), 259–270, doi:10.1088/0959-
612 5309/57/4/301, 1945.

613 Diehl, K., Debertshäuser, M., Eppers, O., Schmithüsen, H., Mitra, S. K. and Borrmann, S.: Particle surface area dependence
614 of mineral dust in immersion freezing mode: Investigations with freely suspended drops in an acoustic levitator and a vertical
615 wind tunnel, *Atmos. Chem. Phys.*, 14(22), 12343–12355, doi:10.5194/acp-14-12343-2014, 2014.

616 van der Does, M., Knippertz, P., Zschenderlein, P., Giles Harrison, R. and Stuut, J. B. W.: The mysterious long-range transport
617 of giant mineral dust particles, *Sci. Adv.*, 4(12), eaau2768, doi:10.1126/sciadv.aau2768, 2018.

618 Du, Y., Xu, X., Chu, M., Guo, Y. and Wang, J.: Air particulate matter and cardiovascular disease: The epidemiological,
619 biomedical and clinical evidence, *J. Thorac. Dis.*, 8(1), E8–E19, doi:10.3978/j.issn.2072-1439.2015.11.37, 2016.

620 Dubovik, O., Holben, B. N., Lapyonok, T., Sinyuk, A., Mishchenko, M. I., Yang, P. and Slutsker, I.: Non-spherical aerosol
621 retrieval method employing light scattering by spheroids, *Geophys. Res. Lett.*, 29(10), 54-1-54-4, doi:10.1029/2001gl014506,
622 2002.

623 Eden, H. F. and Vonnegut, B.: Electrical Breakdown Caused by Dust Motion in Low-Pressure Atmospheres: Considerations
624 for Mars, *Science (80-.)*, 180(4089), 962–963, doi:10.1126/science.180.4089.962, 1973.

625 Escribano, J., Tomaso, E. Di, Jorba, O., Klose, M., Ageitos, M. G., Macchia, F., Amiridis, V., Baars, H., Marinou, E.,
626 Proestakis, E., Urbanneck, C., Althausen, D., Bühl, J., Mamouri, R. and García-pando, C. P.: Assimilating spaceborne lidar
627 dust extinction improves dust forecasts, , (June), 1–36, 2021.

628 Ette, A. I. I.: The effect of the Harmattan dust on atmospheric electric parameters, *J. Atmos. Terr. Phys.*, 33(2), 295–300,
629 doi:https://doi.org/10.1016/0021-9169(71)90208-X, 1971.

630 Garcia-Carreras, L., Parker, D. J., Marsham, J. H., Rosenberg, P. D., Brooks, I. M., Lock, A. P., Marengo, F., Mcquaid, J. B.
631 and Hobby, M.: The turbulent structure and diurnal growth of the Saharan atmospheric boundary layer, *J. Atmos. Sci.*, 72(2),
632 693–713, doi:10.1175/JAS-D-13-0384.1, 2015.

633 Gasteiger, J., Groß, S., Sauer, D., Haarig, M., Ansmann, A. and Weinzierl, B.: Particle settling and vertical mixing in the
634 Saharan Air Layer as seen from an integrated model, lidar, and in situ perspective, *Atmos. Chem. Phys.*, 17(1), 297–311,
635 doi:10.5194/acp-17-297-2017, 2017.

636 Gelaro, R., McCarty, W., Suárez, M. J., Todling, R., Molod, A., Takacs, L., Randles, C. A., Darmenov, A., Bosilovich, M. G.,
637 Reichle, R., Wargan, K., Coy, L., Cullather, R., Draper, C., Akella, S., Buchard, V., Conaty, A., da Silva, A. M., Gu, W., Kim,
638 G. K., Koster, R., Lucchesi, R., Merkova, D., Nielsen, J. E., Partyka, G., Pawson, S., Putman, W., Rienecker, M., Schubert, S.
639 D., Sienkiewicz, M. and Zhao, B.: The modern-era retrospective analysis for research and applications, version 2 (MERRA-
640 2), *J. Clim.*, 30(14), 5419–5454, doi:10.1175/JCLI-D-16-0758.1, 2017.

641 Georgoulias, A. K., Alexandri, G., Kourtidis, K. A., Lelieveld, J. and Zanis, P.: Spatiotemporal variability and contribution of
642 different aerosol types to the aerosol optical depth over the Eastern Mediterranean, , 13853–13884, doi:10.5194/acp-16-13853-
643 2016, 2016.

644 Georgoulias, A. K., Tsikerdekis, A., Amiridis, V., Marinou, E., Benedetti, A., Zanis, P., Alexandri, G., Mona, L., Kourtidis,
645 K. A. and Lelieveld, J.: A 3-D evaluation of the MACC reanalysis dust product over Europe, northern Africa and Middle East
646 using CALIOP/CALIPSO dust satellite observations, *Atmos. Chem. Phys.*, 18(12), 8601–8620, doi:10.5194/acp-18-8601-
647 2018, 2018.

648 Georgoulias, A. K., Boersma, K. F., Van Vliet, J., Zhang, X., Van Der A, R., Zanis, P. and De Laat, J.: Detection of NO₂
649 pollution plumes from individual ships with the TROPOMI/S5P satellite sensor, *Environ. Res. Lett.*, 15(12), doi:10.1088/1748-
650 9326/abc445, 2020.

651 Giannadaki, D., Pozzer, A. and Lelieveld, J.: Modeled global effects of airborne desert dust on air quality and premature
652 mortality, *Atmos. Chem. Phys.*, 14(2), 957–968, doi:10.5194/acp-14-957-2014, 2014.

653 Giles, D. M., Sinyuk, A., Sorokin, M. G., Schafer, J. S., Smirnov, A., Slutsker, I., Eck, T. F., Holben, B. N., Lewis, J. R.,
654 Campbell, J. R., Welton, E. J., Korokin, S. V. and Lyapustin, A. I.: Advancements in the Aerosol Robotic Network (AERONET)
655 Version 3 database - Automated near-real-time quality control algorithm with improved cloud screening for Sun photometer
656 aerosol optical depth (AOD) measurements, *Atmos. Meas. Tech.*, 12(1), 169–209, doi:10.5194/amt-12-169-2019, 2019.

657 Gilliam, R. C. and Pleim, J. E.: Performance Assessment of New Land Surface and Planetary Boundary Layer Physics in the
658 WRF-ARW, *J Appl Meteorol Climatol*, 49, 760–774, <https://doi.org/10.1175/2009JAMC2126.1>, 2010.

659 Ginoux, P., Chin, M., Tegen, I., Goddard, T. and In-, G.: Sources and distributions of dust aerosols simulated with the
660 GOCART model, *J. Geophys. Res.*, 106, 20255–20273, 2001.

661 Ginoux, P.: Effects of nonsphericity on mineral dust modeling, *J. Geophys. Res.*, 108(D2), doi:10.1029/2002jd002516, 2003.

662 Ginoux, P., Prospero, J. M., Gill, T. E., Hsu, N. C. and Zhao, M.: Global-scale attribution of anthropogenic and natural dust
663 sources and their emission rates based on MODIS Deep Blue aerosol products, *Rev. Geophys.*, 50(3), 1–36,
664 doi:10.1029/2012RG000388, 2012.

665 Gkikas, A., Proestakis, E., Amiridis, V., Kazadzis, S., Di Tomaso, E., Tsekeri, A., Marinou, E., Hatzianastassiou, N. and Pérez
666 García-Pando, C.: ModIs Dust AeroSol (MIDAS): A global fine-resolution dust optical depth data set, *Atmos. Meas. Tech.*,
667 14(1), 309–334, doi:10.5194/amt-14-309-2021, 2021.

668 Gkikas, A., Proestakis, E., Amiridis, V., Kazadzis, S., Di Tomaso, E., Marinou, E., Hatzianastassiou, N., Kok, J. F. and García-
669 Pando, C. P.: Quantification of the dust optical depth across spatiotemporal scales with the MIDAS global dataset (2003-2017),
670 *Atmos. Chem. Phys.*, 22(5), 3553–3578, doi:10.5194/acp-22-3553-2022, 2022.

671 Gliß, J., Mortier, A., Schulz, M., Andrews, E., Balkanski, Y., Bauer, S. E., Benedictow, A. M. K., Bian, H., Checa-Garcia, R.,
672 Chin, M., Ginoux, P., Griesfeller, J. J., Heckel, A., Kipling, Z., Kirkevåg, A., Kokkola, H., Laj, P., Le Sager, P., Tronstad
673 Lund, M., Lund Myhre, C., Matsui, H., Myhre, G., Neubauer, D., Van Noije, T., North, P., Olivíe, D. J. L., Rémy, S.,
674 Sogacheva, L., Takemura, T., Tsigaridis, K. and Tsyro, S. G.: AeroCom phase III multi-model evaluation of the aerosol life
675 cycle and optical properties using ground- And space-based remote sensing as well as surface in situ observations, *Atmos.*
676 *Chem. Phys.*, 21(1), 87–128, doi:10.5194/acp-21-87-2021, 2021.

677 Goudie, A. S.: Desert dust and human health disorders, *Environ. Int.*, 63, 101–113, doi:10.1016/j.envint.2013.10.011, 2014.

678 Goudie, A. S. and Middleton, N. J.: *Desert Dust in the Global System.*, 2006.

679 Grell, G. A. and Dévényi, D.: A generalized approach to parameterizing convection combining ensemble and data assimilation
680 techniques, *Geophys Res Lett*, 29, 10–13, <https://doi.org/10.1029/2002GL015311>, 2002.

681 Grell, G. A., Peckham, S. E., Schmitz, R., McKeen, S. A., Frost, G., Skamarock, W. C. and Eder, B.: Fully coupled “online”
682 chemistry within the WRF model, *Atmos. Environ.*, 39(37), 6957–6975, doi:10.1016/j.atmosenv.2005.04.027, 2005.

683 Gu, Z., He, Y., Zhang, Y., Su, J., Zhang, R., Yu, C. W. and Zhang, D.: An overview of triggering mechanisms and
684 characteristics of local strong sandstorms in china and haboobs, *Atmosphere (Basel)*., 12(6), 1–17,
685 doi:10.3390/atmos12060752, 2021.

686 Hansen, J. E. and Travis, L. D.: Light scattering in planetary atmospheres, *Space Sci. Rev.*, 16(4), 527–610,
687 doi:10.1007/BF00168069, 1974.

688 Harb, K., Butt, O., Abdul-jauwad, S. and Al-yami, A. M.: Systems Adaptation for Satellite Signal under Dust , Sand and
689 Gaseous Attenuations, *J. Wirel. Netw. Commun.*, 3(3), 39–49, doi:10.5923/j.jwnc.20130303.03, 2013.

690 Heinold, B., Tegen, I., Esselborn, M., Kandler, K., Knippertz, P., Müller, D., Schladitz, A., Tesche, M., Weinzierl, B.,
691 Ansmann, A., Althausen, D., Laurent, B., Massling, A., Müller, T., Petzold, A., Schepanski, K. and Wiedensohler, A.: Regional
692 Saharan dust modelling during the SAMUM 2006 campaign, *Tellus, Ser. B Chem. Phys. Meteorol.*, 61(1), 307–324,
693 doi:10.1111/j.1600-0889.2008.00387.x, 2009.

694 Hilsenrath, J. and of Standards, U. S. N. B.: Tables of Thermal Properties of Gases: Comprising Tables of Thermodynamic
695 and Transport Properties of Air, Argon, Carbon Dioxide, Carbon Monoxide, Hydrogen, Nitrogen, Oxygen, and Steam, U.S.
696 Department of Commerce, National Bureau of Standards. [online] Available from:
697 <https://books.google.gr/books?id=LK8vaddchE4C>, 1955.

698 Huang, Y., Kok, J. F., Kandler, K., Lindqvist, H., Nousiainen, T., Sakai, T., Adebisi, A. and Jokinen, O.: Climate Models and
699 Remote Sensing Retrievals Neglect Substantial Desert Dust Asphericity, *Geophys. Res. Lett.*, 47(6), 1–11,
700 doi:10.1029/2019GL086592, 2020,

701 Huneus, N., Schulz, M., Balkanski, Y., Griesfeller, J., Prospero, J., Kinne, S., Bauer, S., Boucher, O., Chin, M., Dentener, F.,
702 Diehl, T., Easter, R., Fillmore, D., Ghan, S., Ginoux, P., Grini, A., Horowitz, L., Koch, D., Krol, M. C., Landing, W., Liu, X.,
703 Mahowald, N., Miller, R., Morcrette, J.-J., Myhre, G., Penner, J., Perlwitz, J., Stier, P., Takemura, T. and Zender, C. S.: Global
704 dust model intercomparison in AeroCom phase I, *Atmos. Chem. Phys.*, 11(15), 7781–7816, doi:10.5194/acp-11-7781-2011,
705 2011.

706 Jayaratne, E. R.: Charge separation during the impact of sand on ice and its relevance to theories of thunderstorm electrification,
707 *Atmos. Res.*, 26(5), 407–424, doi:[https://doi.org/10.1016/0169-8095\(91\)90061-Z](https://doi.org/10.1016/0169-8095(91)90061-Z), 1991.

708 Jennings, S. G.: The mean free path in air, *J. Aerosol Sci.*, 19(2), 159–166, doi:10.1016/0021-8502(88)90219-4, 1988.

709 Jickells, T. D., An, Z. S., Andersen, K. K., Baker, A. R., Bergametti, C., Brooks, N., Cao, J. J., Boyd, P. W., Duce, R. A.,
710 Hunter, K. A., Kawahata, H., Kubilay, N., LaRoche, J., Liss, P. S., Mahowald, N., Prospero, J. M., Ridgwell, A. J., Tegen, I.

711 and Torres, R.: Global iron connections between desert dust, ocean biogeochemistry, and climate, *Science* (80-.), 308(5718),
712 67–71, doi:10.1126/science.1105959, 2005.

713 Jickells, T., Boyd, P. and Hunter, K. A.: Biogeochemical Impacts of Dust on the Global Carbon Cycle, in *Mineral Dust: A*
714 *Key Player in the Earth System*, edited by P. Knippertz and J.-B. W. Stuut, pp. 359–384, Springer Netherlands, Dordrecht.,
715 2014.

716 Kandler, K., et al.: Size distribution, mass concentration, chemical and mineralogical composition and derived optical
717 parameters of the boundary layer aerosol at Tinfou, Morocco, during SAMUM 2006, *Tellus B*, 61, 32–50,
718 <https://doi.org/10.1111/j.1600-0889.2008.00385.x>, 2009.

719 Knippertz, P. and Stuut, J. B. W.: Mineral dust: A key player in the earth system, *Miner. Dust A Key Play. Earth Syst.*, 1–509,
720 doi:10.1007/978-94-017-8978-3, 2014.

721 Kok, J. F.: An improved parameterization of wind-blown sand flux on Mars that includes the effect of hysteresis, *Geophys.*
722 *Res. Lett.*, 37(12), doi:10.1029/2010GL043646, 2010.

723 Kok, J. F.: A scaling theory for the size distribution of emitted dust aerosols suggests climate models underestimate the size
724 of the global dust cycle, *Proc. Natl. Acad. Sci. U. S. A.*, 108(3), 1016–1021, doi:10.1073/pnas.1014798108, 2011.

725 Kok, J. F., Adebisi, A. A., Albani, S., Balkanski, Y., Checa-Garcia, R., Chin, M., Colarco, P. R., Hamilton, D. S., Huang, Y.,
726 Ito, A., Klose, M., Leung, D. M., Li, L., Mahowald, N. M., Miller, R. L., Obiso, V., Pérez García-Pando, C., Rocha-Lima, A.,
727 Wan, J. S. and Whicker, C. A.: Improved representation of the global dust cycle using observational constraints on dust
728 properties and abundance, *Atmos. Chem. Phys.*, 21(10), 8127–8167, doi:10.5194/acp-21-8127-2021, 2021.

729 Konsta, D., Biniotoglou, I., Gkikas, A., Solomos, S., Marinou, E., Proestakis, E., Basart, S., García-Pando, C. P., El-Askary,
730 H. and Amiridis, V.: Evaluation of the BSC-DREAM8b regional dust model using the 3D LIVAS-CALIPSO product, *Atmos.*
731 *Environ.*, 195, 46–62, doi:10.1016/j.atmosenv.2018.09.047, 2018.

732 Kosmopoulos, P. G., Kazadzis, S., El-Askary, H., Taylor, M., Gkikas, A., Proestakis, E., Kontoes, C. and El-Khayat, M. M.:
733 Earth-observation-based estimation and forecasting of particulate matter impact on solar energy in Egypt, *Remote Sens.*,
734 10(12), 1–23, doi:10.3390/rs10121870, 2018.

735 Krauss, C. E., Horányi, M. and Robertson, S.: Experimental evidence for electrostatic discharging of dust near the surface of
736 Mars, *New J. Phys.*, 5, doi:10.1088/1367-2630/5/1/370, 2003.

737 LeGrand, S. L., Polashenski, C., Letcher, T. W., Creighton, G. A., Peckham, S. E. and Cetola, J. D.: The AFWA dust emission
738 scheme for the GOCART aerosol model in WRF-Chem v3.8.1, *Geosci. Model Dev.*, 12(1), 131–166, doi:10.5194/gmd-12-
739 131-2019, 2019.

740 Li, J. and Osada, K.: Preferential settling of elongated mineral dust particles in the atmosphere, , 34, 17807,
741 doi:10.1029/2007GL030262, 2007.

742 Liu, D., Taylor, J. W., Crosier, J., Marsden, N., Bower, K. N., Lloyd, G., Ryder, C. L., Brooke, J. K., Cotton, R., Marenco, F.,
743 Blyth, A., Cui, Z., Estelles, V., Gallagher, M., Coe, H. and Choulaton, T. W.: Aircraft and ground measurements of dust
744 aerosols over the west African coast in summer 2015 during ICE-D and AER-D, *Atmos. Chem. Phys.*, 18(5), 3817–3838,
745 doi:10.5194/acp-18-3817-2018, 2018.

746 Loth, E.: Drag of non-spherical solid particles of regular and irregular shape, *Powder Technol.*, 182(3), 342–353,
747 doi:10.1016/j.powtec.2007.06.001, 2008.

748 Mahowald, N., Albani, S., Kok, J. F., Engelstaeder, S., Scanza, R., Ward, D. S. and Flanner, M. G.: The size distribution of
749 desert dust aerosols and its impact on the Earth system, *Aeolian Res.*, 15, 53–71, doi:10.1016/j.aeolia.2013.09.002, 2014.

750 Mallios, S. A., Drakaki, E. and Amiridis, V.: Effects of dust particle sphericity and orientation on their gravitational settling
751 in the earth’s atmosphere, *J. Aerosol Sci.*, 150(April), 105634, doi:10.1016/j.jaerosci.2020.105634, 2020.

752 Mallios, S. A., Papangelis, G., Hloupis, G., Papaioannou, A., Daskalopoulou, V. and Amiridis, V.: Modeling of Spherical Dust
753 Particle Charging due to Ion Attachment, *Front. Earth Sci.*, 9(August), 1–22, doi:10.3389/feart.2021.709890, 2021a.

754 Mallios, S. A., Daskalopoulou, V. and Amiridis, V.: Orientation of non spherical prolate dust particles moving vertically in
755 the Earth’s atmosphere, *J. Aerosol Sci.*, 151(November 2019), 105657, doi:10.1016/j.jaerosci.2020.105657, 2021b.

756 Mallios, S. A., Daskalopoulou, V. and Amiridis, V.: Modeling of the electrical interaction between desert dust particles and
757 the Earth’s atmosphere, *J. Aerosol Sci.*, 165, 106044, doi:https://doi.org/10.1016/j.jaerosci.2022.106044, 2022.

758 Maring, H.: Mineral dust aerosol size distribution change during atmospheric transport, *J. Geophys. Res.*, 108(D19), 8592,
759 doi:10.1029/2002JD002536, 2003.

760 Marinou, E., Amiridis, V., Biniotoglou, I., Tsikerdekis, A., Solomos, S., Proestakis, E., Konsta, Di., Papagiannopoulos, N.,
761 Tsekeri, A., Vlastou, G., Zanis, P., Balis, Di., Wandinger, U. and Ansmann, A.: Three-dimensional evolution of Saharan dust
762 transport towards Europe based on a 9-year EARLINET-optimized CALIPSO dataset, *Atmos. Chem. Phys.*, 17(9), 5893–
763 5919, doi:10.5194/acp-17-5893-2017, 2017.

764 Marinou, E., Tesche, M., Nenes, A., Ansmann, A., Schrod, J., Mamali, D., Tsekeri, A., Pikridas, M., Baars, H., Engelmann,
765 R., Voudouri, K. A., Solomos, S., Sciare, J., Groß, S., Ewald, F. and Amiridis, V.: Retrieval of ice-nucleating particle
766 concentrations from lidar observations and comparison with UAV in situ measurements, *Atmos. Chem. Phys.*, 19(17), 11315–
767 11342, doi:10.5194/acp-19-11315-2019, 2019.

768 Meng, J., Huang, Y., Leung, D. M., Li, L., Adebisi, A. A., Ryder, C. L., Mahowald, N. M. and Kok, J. F.: Improved
769 Parameterization for the Size Distribution of Emitted Dust Aerosols Reduces Model Underestimation of Super Coarse Dust,
770 *Geophys. Res. Lett.*, 49(8), e2021GL097287, doi:<https://doi.org/10.1029/2021GL097287>, 2022.

771 Mie, G.: Beiträge zur Optik trüber Medien, speziell kolloidaler Metallösungen, *Ann. Phys.*, 330(3), 377–445,
772 doi:<https://doi.org/10.1002/andp.19083300302>, 1908.

773 Mills, A. A.: Dust clouds and frictional generation of glow discharges on Mars, *Nature*, 268(5621), 614,
774 doi:10.1038/268614a0, 1977.

775 Nakanishi, M. and Niino, H.: An improved Mellor-Yamada Level-3 model: Its numerical stability and application to a regional
776 prediction of advection fog, *Boundary Layer Meteorol*, 119, 397–407, <https://doi.org/10.1007/s10546-005-9030-8>, 2006.

777 Nickovic, S., Cvetkovic, B., Petković, S., Amiridis, V., Pejanović, G., Solomos, S., Marinou, E. and Nikolic, J.: Cloud icing
778 by mineral dust and impacts to aviation safety, *Sci. Rep.*, 11(1), 6411, doi:10.1038/s41598-021-85566-y, 2021.

779 Nicoll, K. A., Harrison, R. G. and Ulanowski, Z.: Observations of Saharan dust layer electrification, *Environ. Res. Lett.*, 6(1),
780 1–8, doi:10.1088/1748-9326/6/1/014001, 2011.

781 O’Sullivan, D., Marenco, F., Ryder, C., Pradhan, Y., Kipling, Z., Johnson, B., Benedetti, A., Brooks, M., McGill, M., Yorks,
782 J. and Selmer, P.: Models transport Saharan dust too low in the atmosphere compared to observations, *Atmos. Chem. Phys.*
783 *Discuss.*, 1–47, doi:10.5194/acp-2020-57, 2020.

784 Okin, G. S., Mahowald, N., Chadwick, O. A. and Artaxo, P.: Impact of desert dust on the biogeochemistry of phosphorus in
785 terrestrial ecosystems, *Global Biogeochem. Cycles*, 18(2), doi:10.1029/2003GB002145, 2004.

786 Pérez, C., Nickovic, S., Pejanovic, G., Baldasano, J. M. and Özsoy, E.: Interactive dust-radiation modeling: A step to improve
787 weather forecasts, *J. Geophys. Res.*, 111(D16), D16206, doi:10.1029/2005JD006717, 2006.

788 Petters, M. D. and Kreidenweis, S. M.: A single parameter representation of hygroscopic growth and cloud condensation
789 nucleus activity-Part 3: Including surfactant partitioning, *Atmos. Chem. Phys.*, 13(2), 1081–1091, doi:10.5194/acp-13-1081-
790 2013, 2013.

791 Proestakis, E., Amiridis, V., Marinou, E., Georgoulas, A. K., Solomos, S., Kazadzis, S., Chimot, J., Che, H., Alexandri, G.,
792 Binietoglou, I., Daskalopoulou, V., Kourtidis, K. A., De Leeuw, G. and Van Der A, R. J.: Nine-year spatial and temporal
793 evolution of desert dust aerosols over South and East Asia as revealed by CALIOP, *Atmos. Chem. Phys.*, 18(2), 1337–1362,
794 doi:10.5194/acp-18-1337-2018, 2018.

795 Prospero, J. M., Bonatti, E., Schubert, C. and Carlson, T. N.: Dust in the Caribbean atmosphere traced to an African dust storm,
796 *Earth Planet. Sci. Lett.*, 9(3), 287–293, doi:10.1016/0012-821X(70)90039-7, 1970.

797 Prospero, J. M., Ginoux, P., Torres, O., Nicholson, S. E. and Gill, T. E.: Environmental characterization of global sources of
798 atmospheric soil dust identified with the Nimbus 7 Total Ozone Mapping Spectrometer (TOMS) absorbing aerosol product,
799 *Rev. Geophys.*, 40(1), 2-1-2–31, doi:10.1029/2000RG000095, 2002.

800 Renard, J. B., Dulac, F., Durand, P., Bourgeois, Q., Denjean, C., Vignelles, D., Couté, B., Jeannot, M., Verdier, N. and Mallet,
801 M.: In situ measurements of desert dust particles above the western Mediterranean Sea with the balloon-borne Light Optical
802 Aerosol Counter/sizer (LOAC) during the ChArMEx campaign of summer 2013, *Atmos. Chem. Phys.*, 18(5), 3677–3699,
803 doi:10.5194/acp-18-3677-2018, 2018.

804 Roberts, A. J., Marsham, J. H., Knippertz, P., Parker, D. J., Bart, M., Garcia-Carreras, L., Hobby, M., McQuaid, J. B.,
805 Rosenberg, P. D. and Walker, D.: New Saharan wind observations reveal substantial biases in analysed dust-generating winds,
806 *Atmos. Sci. Lett.*, 18(9), 366–372, doi:10.1002/asl.765, 2017.

807 Rycroft, M. J., Harrison, R. G., Nicoll, K. A. and Mareev, E. A.: An Overview of Earth’s Global Electric Circuit and
808 Atmospheric Conductivity, *Space Sci. Rev.*, 137(1), 83–105, doi:10.1007/s11214-008-9368-6, 2008.

809 Ryder, C. L., Highwood, E. J., Lai, T. M., Sodemann, H. and Marsham, J. H.: Impact of atmospheric transport on the evolution
810 of microphysical and optical properties of Saharan dust, *Geophys. Res. Lett.*, 40(10), 2433–2438, doi:10.1002/grl.50482,
811 2013a.

812 Ryder, C. L., Highwood, E. J., Rosenberg, P. D., Trembath, J., Brooke, J. K., Bart, M., Dean, A., Crosier, J., Dorsey, J.,
813 Brindley, H., Banks, J., Marsham, J. H., McQuaid, J. B., Sodemann, H. and Washington, R.: Optical properties of Saharan
814 dust aerosol and contribution from the coarse mode as measured during the Fennec 2011 aircraft campaign, *Atmos. Chem.*
815 *Phys.*, 13(1), 303–325, doi:10.5194/acp-13-303-2013, 2013b.

816 Ryder, C. L., Marengo, F., Brooke, J. K., Estelles, V., Cotton, R., Formenti, P., McQuaid, J. B., Price, H. C., Liu, D., Ausset,
817 P., Rosenberg, P. D., Taylor, J. W., Choulaton, T., Bower, K., Coe, H., Gallagher, M., Crosier, J., Lloyd, G., Highwood, E. J.
818 and Murray, B. J.: Coarse-mode mineral dust size distributions, composition and optical properties from AER-D aircraft
819 measurements over the tropical eastern Atlantic, *Atmos. Chem. Phys.*, 18(23), 17225–17257, doi:10.5194/acp-18-17225-2018,
820 2018.

821 Ryder, C. L., Highwood, E. J., Walser, A., Seibert, P., Philipp, A. and Weinzierl, B.: Coarse and giant particles are ubiquitous
822 in Saharan dust export regions and are radiatively significant over the Sahara, *Atmos. Chem. Phys.*, 19(24), 15353–15376,
823 doi:10.5194/acp-19-15353-2019, 2019.

824 Sanjeevi, S. K. P., Kuipers, J. A. M. and Padding, J. T.: Drag, lift and torque correlations for non-spherical particles from
825 Stokes limit to high Reynolds numbers, *Int. J. Multiph. Flow*, 106, 325–337, doi:10.1016/j.ijmultiphaseflow.2018.05.011,
826 2018.

827 Shao, B., Liu, G. R., Lin, T., Xu, G. X. and Yan, X.: Rotation and orientation of irregular particles in viscous fluids using the
828 gradient smoothed method (GSM), *Eng. Appl. Comput. Fluid Mech.*, 11(1), 557–575, doi:10.1080/19942060.2017.1329169,
829 2017.

830 Sinyuk, A., Holben, B. N., Eck, T. F., Giles, D. M., Slutsker, I., Korokin, S., Schafer, J. S., Smirnov, A., Sorokin, M. and
831 Lyapustin, A.: The AERONET Version 3 aerosol retrieval algorithm, associated uncertainties and comparisons to Version 2,
832 *Atmos. Meas. Tech.*, 13(6), 3375–3411, doi:10.5194/amt-13-3375-2020, 2020.

833 Solomos, S., Kallos, G., Kushta, J., Astitha, M., Tremback, C., Nenes, A. and Levin, Z.: An integrated modeling study on the
834 effects of mineral dust and sea salt particles on clouds and precipitation, *Atmos. Chem. Phys.*, 11(2), 873–892,
835 doi:10.5194/acp-11-873-2011, 2011.

836 Solomos, S., Ansmann, A., Mamouri, R. E., Biniotoglou, I., Patlakas, P., Marinou, E. and Amiridis, V.: Remote sensing and
837 modelling analysis of the extreme dust storm hitting the Middle East and eastern Mediterranean in September 2015, *Atmos.*
838 *Chem. Phys.*, 17(6), 4063–4079, doi:10.5194/acp-17-4063-2017, 2017.

839 Solomos, S., Kalivitis, N., Mihalopoulos, N., Amiridis, V., Kouvarakis, G., Gkikas, A., Biniotoglou, I., Tsekeri, A., Kazadzis,
840 S., Kottas, M., Pradhan, Y., Proestakis, E., Nastos, P. T. and Marengo, F.: From tropospheric folding to Khamsin and Foehn
841 winds: How atmospheric dynamics advanced a record-breaking dust episode in Crete, *Atmosphere (Basel)*, 9(7),
842 doi:10.3390/atmos9070240, 2018.

843 Stockdale, A., Krom, M. D., Mortimer, R. J. G., Benning, L. G., Carslaw, K. S., Herbert, R. J., Shi, Z., Myriokefalitakis, S.,
844 Kanakidou, M. and Nenes, A.: Understanding the nature of atmospheric acid processing of mineral dusts in supplying
845 bioavailable phosphorus to the oceans, *Proc. Natl. Acad. Sci. U. S. A.*, 113(51), 14639–14644, doi:10.1073/pnas.1608136113,
846 2016.

847 Tagliabue, A., Bowie, A. R., Boyd, P. W., Buck, K. N., Johnson, K. S. and Saito, M. A.: The integral role of iron in ocean
848 biogeochemistry, *Nature*, 543(7643), 51–59, doi:10.1038/nature21058, 2017.

849 Tesche, M., Ansmann, A., Müller, D., Althausen, D., Mattis, I., Heese, B., Freudenthaler, V., Wiegner, M., Esselborn, M.,
850 Pisani, G. and Knippertz, P.: Vertical profiling of Saharan dust with Raman lidars and airborne HSRL in southern Morocco
851 during SAMUM, *Tellus, Ser. B Chem. Phys. Meteorol.*, 61(1), 144–164, doi:10.1111/j.1600-0889.2008.00390.x, 2009.

852 Textor, C., Schulz, M., Guibert, S., Kinne, S., Balkanski, Y., Bauer, S., Berntsen, T., Berglen, T., Boucher, O., Chin, M.,
853 Dentener, F., Diehl, T., Easter, R., Feichter, H., Fillmore, D., Ghan, S., Ginoux, P., Gong, S., Grini, A., Hendricks, J., Horowitz,
854 L., Huang, P., Isaksen, I., Iversen, T., Kloster, S., Koch, D., Kirkevåg, A., Kristjansson, J. E., Krol, M., Lauer, A., Lamarque,
855 J. F., Liu, X., Montanaro, V., Myhre, G., Penner, J., Pitari, G., Reddy, S., Seland, Stier, P., Takemura, T. and Tie, X.: Analysis
856 and quantification of the diversities of aerosol life cycles within AeroCom, *Atmos. Chem. Phys.*, 6(7), 1777–1813,
857 doi:10.5194/acp-6-1777-2006, 2006.

858 Toth III, J., Rajupet, S., Squire, H., Volbers, B., Zhou, J., Xie, L., Sankaran, R. M. and Lacks, D.: Electrostatic forces alter
859 particle size distributions in atmospheric dust, *Atmos. Chem. Phys. Discuss.*, 1–14, doi:10.5194/acp-2019-650, 2019.

860 Tsekeri, A., Amiridis, V., Tsihla, M., Fountoulakis, I., Nersesian, A., Proestakis, E., Gkikas, A., Papachristopoulou, K.,
861 Barlakas, V., and Kazadzis, S.: The effect of large dust size on solar radiation fluxes, *International Radiation Symposium*,
862 Thessaloniki, Greece, 4-8 July 2022.

863 Tsikerdekis, A., Zanis, P., Steiner, A. L., Solmon, F., Amiridis, V., Marinou, E., Katragkou, E., Karacostas, T. and Foret, G.:
864 Impact of dust size parameterizations on aerosol burden and radiative forcing in RegCM4, *Atmos. Chem. Phys.*, 17(2), 769–
865 791, doi:10.5194/acp-17-769-2017, 2017.

866 Twohy, C. H., Kreidenweis, S. M., Eidhammer, T., Browell, E. V., Heymsfield, A. J., Bansemer, A. R., Anderson, B. E., Chen,
867 G., Ismail, S., DeMott, P. J. and Van Den Heever, S. C.: Saharan dust particles nucleate droplets in eastern Atlantic clouds,
868 *Geophys. Res. Lett.*, 36(1), 1–6, doi:10.1029/2008GL035846, 2009.

869 U.S. Standard Atmosphere, 1962, U.S. Government Printing Office, Washington, D.C.,
870 1962, [https://www.ngdc.noaa.gov/stp/space-weather/online-publications/miscellaneous/us-standard-atmosphere-1976/us-](https://www.ngdc.noaa.gov/stp/space-weather/online-publications/miscellaneous/us-standard-atmosphere-1976/us-standard-atmosphere_st76-1562_noaa.pdf)
871 [standard-atmosphere_st76-1562_noaa.pdf](https://www.ngdc.noaa.gov/stp/space-weather/online-publications/miscellaneous/us-standard-atmosphere-1976/us-standard-atmosphere_st76-1562_noaa.pdf)

872 Versteeg H. K. & Malalasekera W. (2007). *An introduction to computational fluid dynamics : the finite volume method* (2nd
873 ed.). Pearson Education.

874 Weinzierl, B., Petzold, A., Esselborn, M., Wirth, M., Rasp, K., Kandler, K., SchütZ, L., Koepke, P. and Fiebig, M.: Airborne
875 measurements of dust layer properties, particle size distribution and mixing state of Saharan dust during SAMUM 2006, *Tellus*
876 *B Chem. Phys. Meteorol.*, 61(1), 96–117, doi:10.1111/j.1600-0889.2008.00392.x, 2009.

877 Weinzierl, B., Sauer, D., Esselborn, M., Petzold, A., Veira, A., Rose, M., Mund, S., Wirth, M., Ansmann, A., Tesche, M.,
878 Gross, S. and Freudenthaler, V.: Microphysical and optical properties of dust and tropical biomass burning aerosol layers in
879 the Cape Verde region-an overview of the airborne in situ and lidar measurements during SAMUM-2, *Tellus, Ser. B Chem.*
880 *Phys. Meteorol.*, 63(4), 589–618, doi:10.1111/j.1600-0889.2011.00566.x, 2011.

881 Weinzierl, B., Sauer, D., Minikin, A., Reitebuch, O., Dahlkötter, F., Mayer, B., Emde, C., Tegen, I., Gasteiger, J., Petzold, A.,
882 Veira, A., Kueppers, U. and Schumann, U.: On the visibility of airborne volcanic ash and mineral dust from the pilot's
883 perspective in flight, *Phys. Chem. Earth*, 45–46, 87–102, doi:10.1016/j.pce.2012.04.003, 2012.

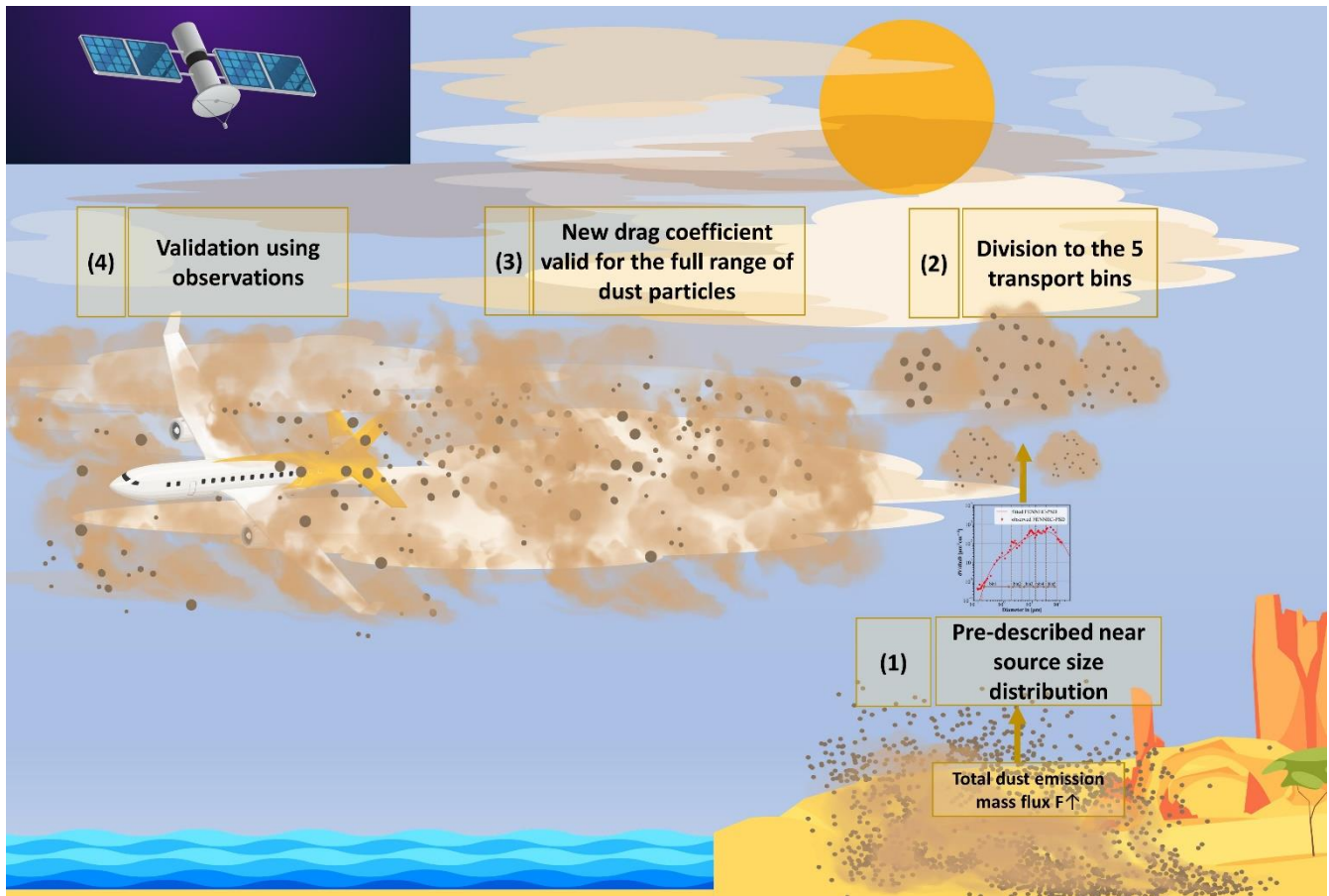
884 Weinzierl, B., Ansmann, A., Prospero, J. M., Althausen, D., Benker, N., Chouza, F., Dollner, M., Farrell, D., Fomba, W. K.,
885 Freudenthaler, V., Gasteiger, J., Groß, S., Haarig, M., Heinold, B., Kandler, K., Kristensen, T. B., Mayol-Bracero, O. L.,
886 Müller, T., Reitebuch, O., Sauer, D., Schäfler, A., Schepanski, K., Spanu, A., Tegen, I., Toledano, C. and Walser, A.: The

887 Saharan aerosol long-range transport and aerosol-cloud-interaction experiment: Overview and selected highlights, Bull. Am.
888 Meteorol. Soc., 98(7), 1427–1451, doi:10.1175/BAMS-D-15-00142.1, 2017.

889 Winker, D. M., Vaughan, M. A., Omar, A., Hu, Y., Powell, K. A., Liu, Z., Hunt, W. H. and Young, S. A.: Overview of the
890 CALIPSO Mission and CALIOP Data Processing Algorithms, J. Atmos. Ocean. Technol., 26(11), 2310–2323,
891 doi:10.1175/2009JTECHA1281.1, 2009.

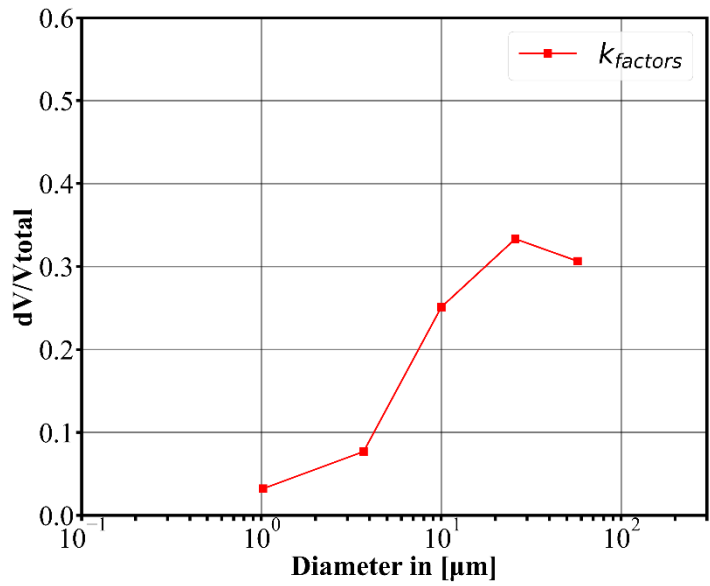
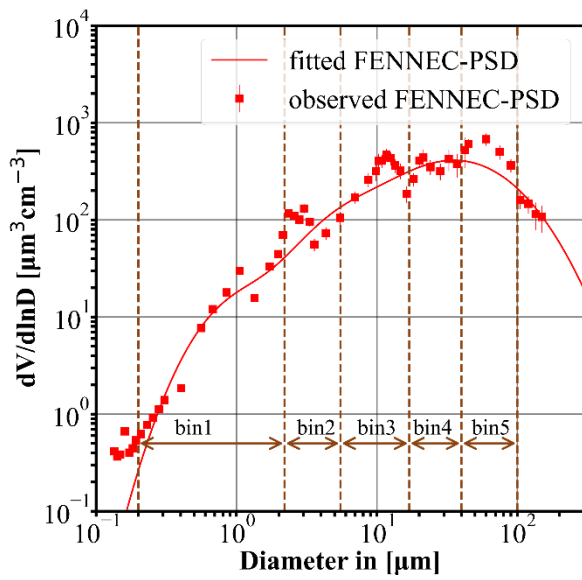
892 Zastawny, M., Mallouppas, G., Zhao, F. and van Wachem, B.: Derivation of drag and lift force and torque coefficients for
893 non-spherical particles in flows, Int. J. Multiph. Flow, 39, 227–239, doi:10.1016/j.ijmultiphaseflow.2011.09.004, 2012.

894



895

896 **Figure 1: The structure of the presented work. Steps (1), (2) and (3) correspond to the appropriate modifications**
897 **implemented in the WRF-Chem GOCART-AFWA dust scheme, for the inclusion of the giant dust particles and the**
898 **development of WRF-L. Step (4) refers to model validation activities.**



899

900

901

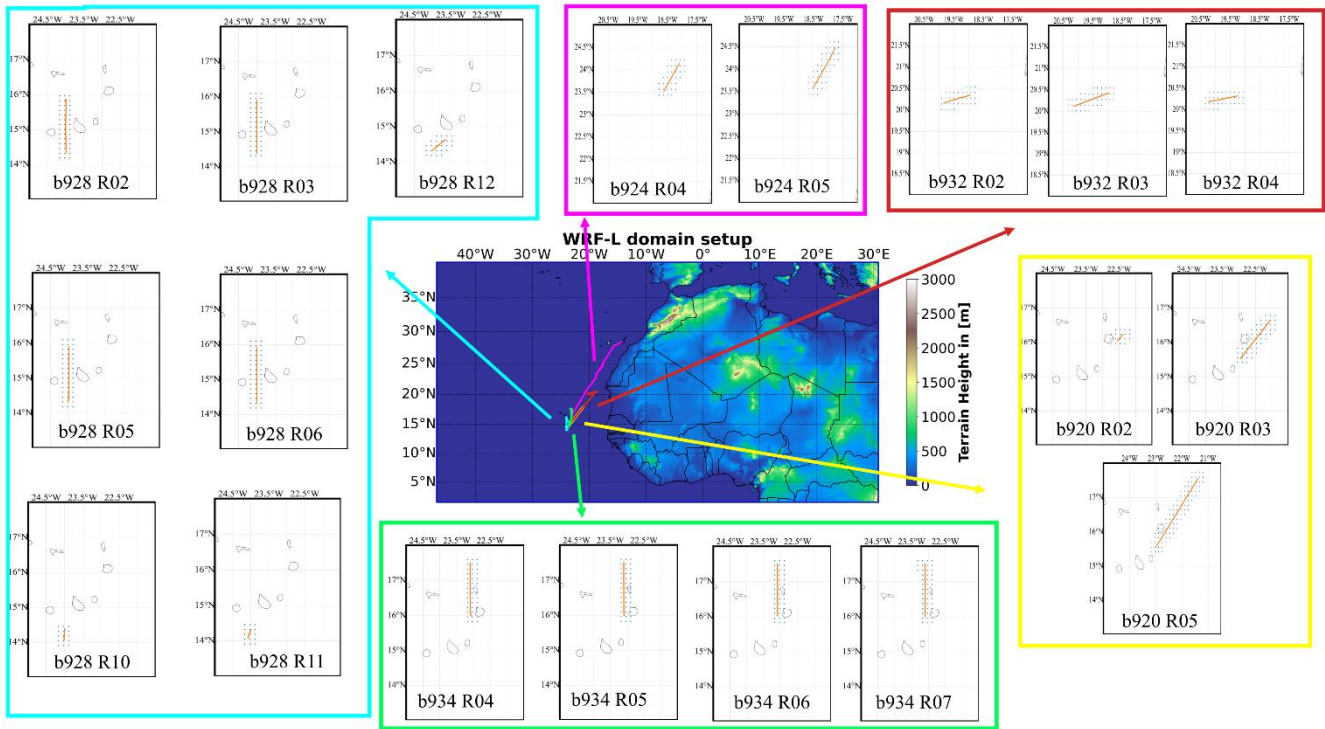
902

903

904

905

Figure 2: Prescribed dust size distribution used in the WRF-L for the distribution of total dust mass to the transport model size bins: (a) “observed FENNEC-PSD” ($\mu\text{m}^3\text{cm}^{-3}$) (red squares), and the respective “fitted FENNEC-PSD” (red solid line). The “observed FENNEC-PSD” corresponds to the PSD observations at 1km, obtained by averaging profile measured data of freshly uplifted dust cases, over 500m. The arrows indicate the model transport size bins in WRF-L. Error bars indicate the standard deviation of the observed values (b) The k_{factors} of the transport size bins calculated based on “fitted FENNEC-PSD”, provide the mass fraction of the emitted dust for each bin.



906

907

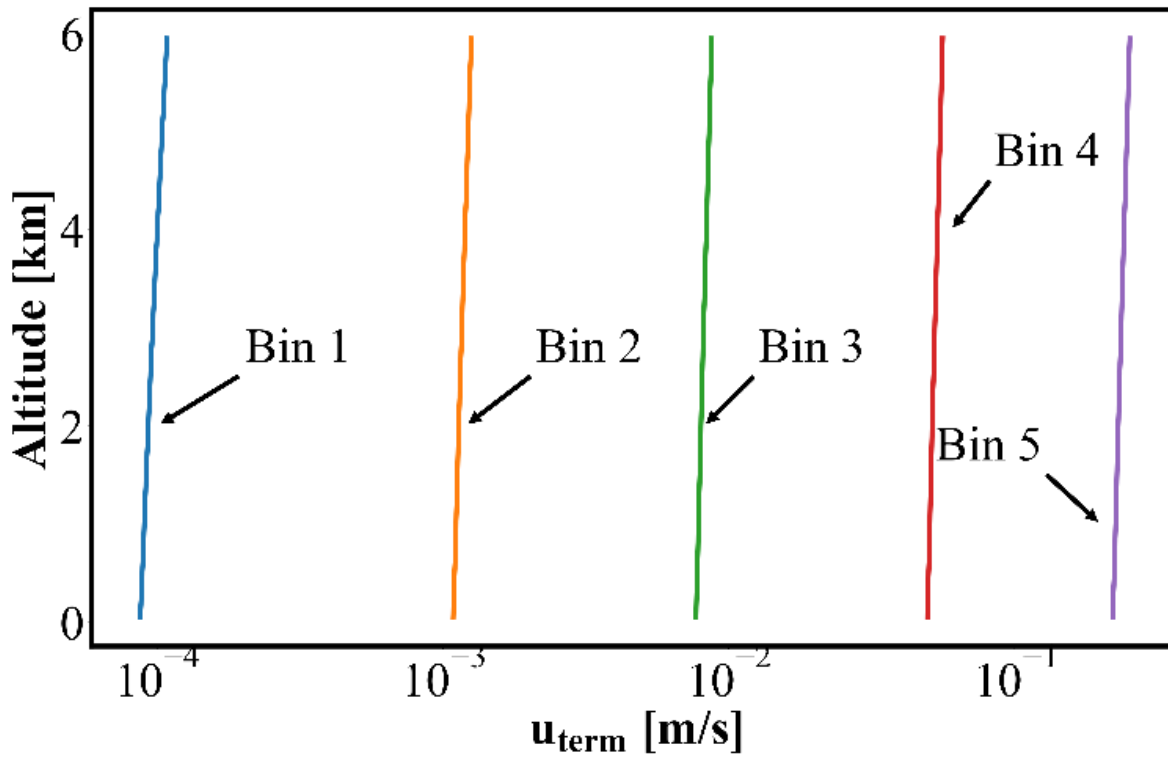
Figure 3: Domain and topography map of the WRF-L model simulations, with a horizontal grid spacing of 15km, and 70 vertical levels. The tracks of the AER-D flights, used in this study (b920, b924, b928, b932 and b934), are depicted in the central plot with different colors. In the surrounding maps, the orange dots indicate the aircraft tracks of each flight RUN. The blue dots correspond to the collocated model grid points.

908

909

910

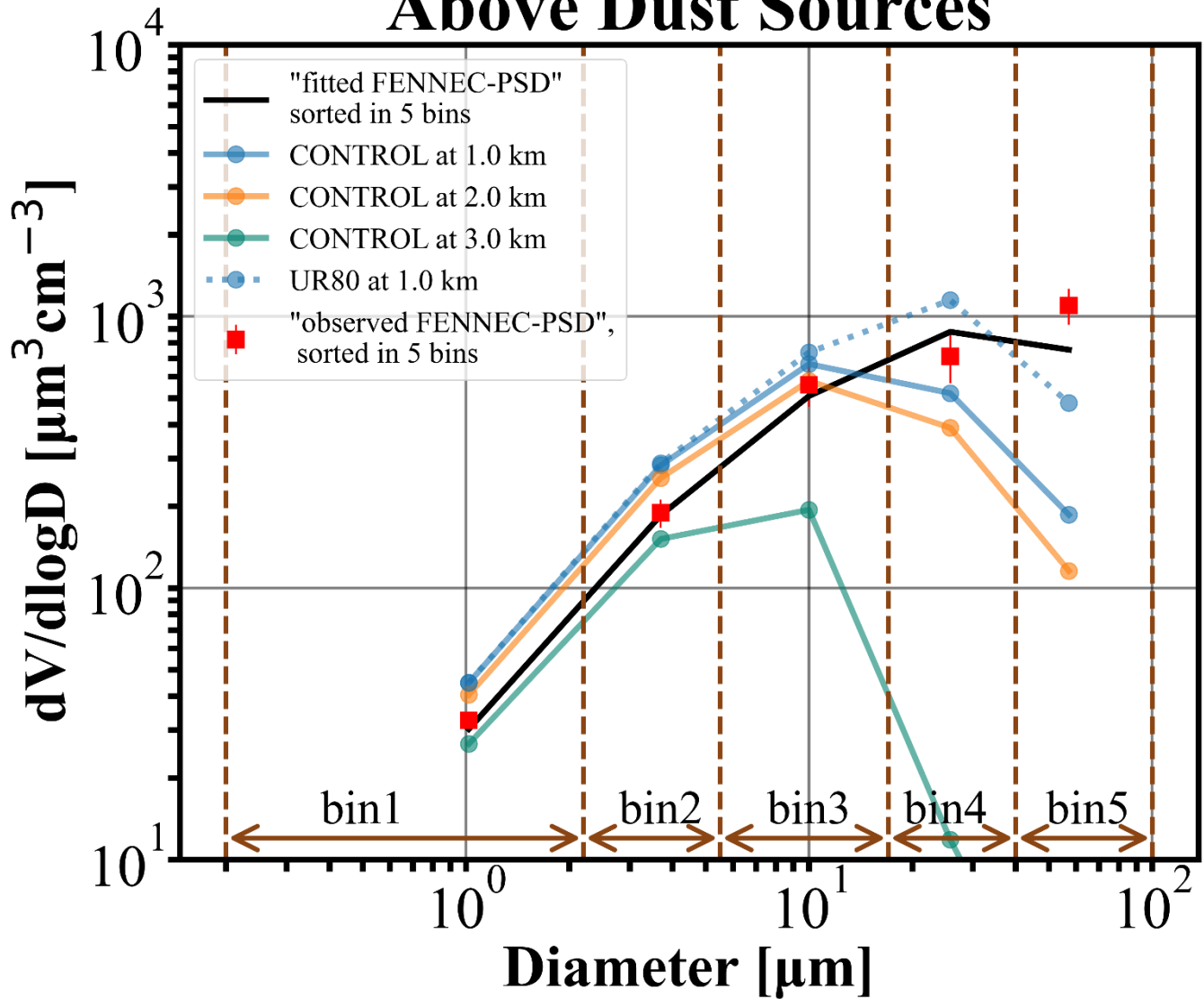
Settling Velocities



911

912 **Figure 4: Terminal velocities of the CONTROL experiment, averaged for the simulation time and the domain. Each**
913 **colored line corresponds to one of the new model size bins, with blue: Bin 1, orange: Bin 2, green: Bin 3, red: Bin 4 and**
914 **purple: Bin 5.**

Above Dust Sources



915

916

917

918

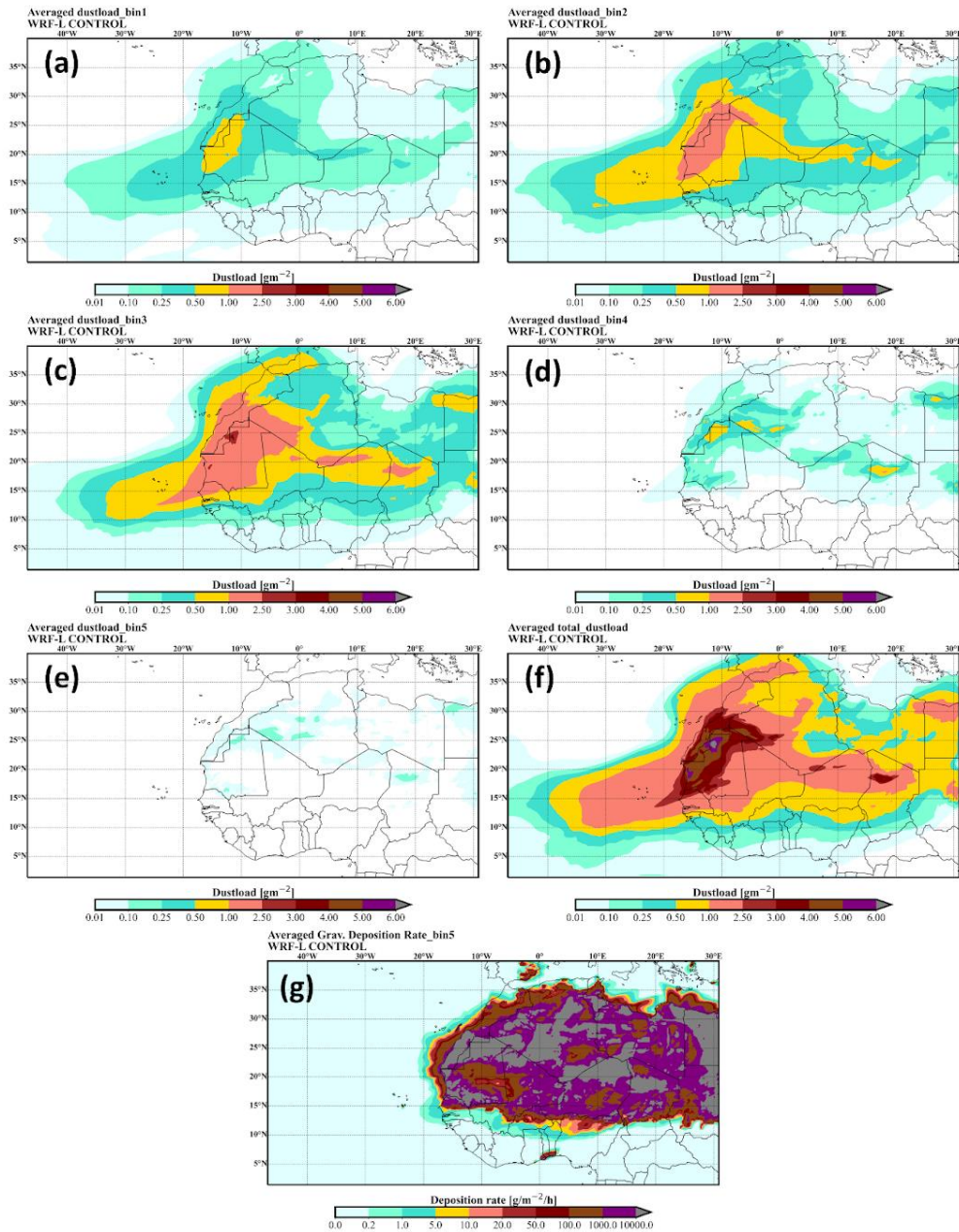
919

920

921

922

Figure 5: Dust size distribution above an emission model grid point (latitude=24.9° and longitude=9.2°) in Mali, on 11/08/2015 at 14UTC. Blue solid line: the dust PSD of the CONTROL run interpolated at 1 km altitude above the dust source, orange solid line: the dust PSD of the CONTROL run interpolated at 2 km altitude above dust source, green solid line: the dust PSD of the CONTROL run interpolated at 3 km altitude above dust source, blue dotted line: the dust PSD of the UR80 run interpolated at 1 km altitude above the dust source and red squares: the “observed FENNEC-PSD” at 1 km altitude (sorted in 5 bins) , black squares the “fitted FENNEC-PSD” at 1km (sorted in 5 bins) which has been used for the distribution of the model emission to the five size bins.



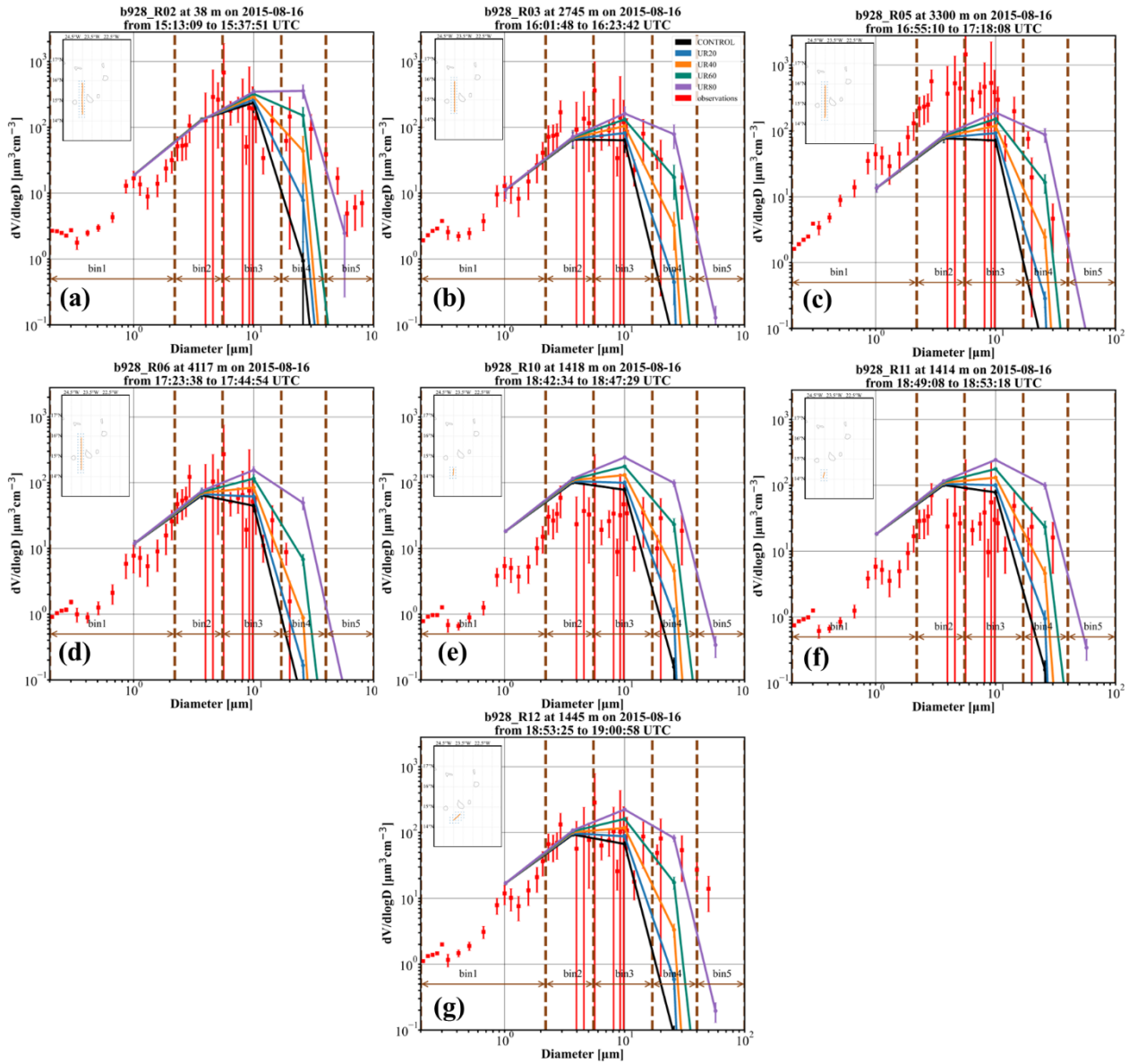
923

924

925

926

Figure 6: The dust load provided by the model, averaged for the whole simulation period, for (a) bin 1, (b) bin 2, (c) bin 3, (d) bin 4, (e) bin 5, and (f) the whole range of the PSD. The dust load is in g/m^2 . (g) The gravitational deposition rate for bin 5 in $\text{g/m}^2/\text{h}$.



927

928

929

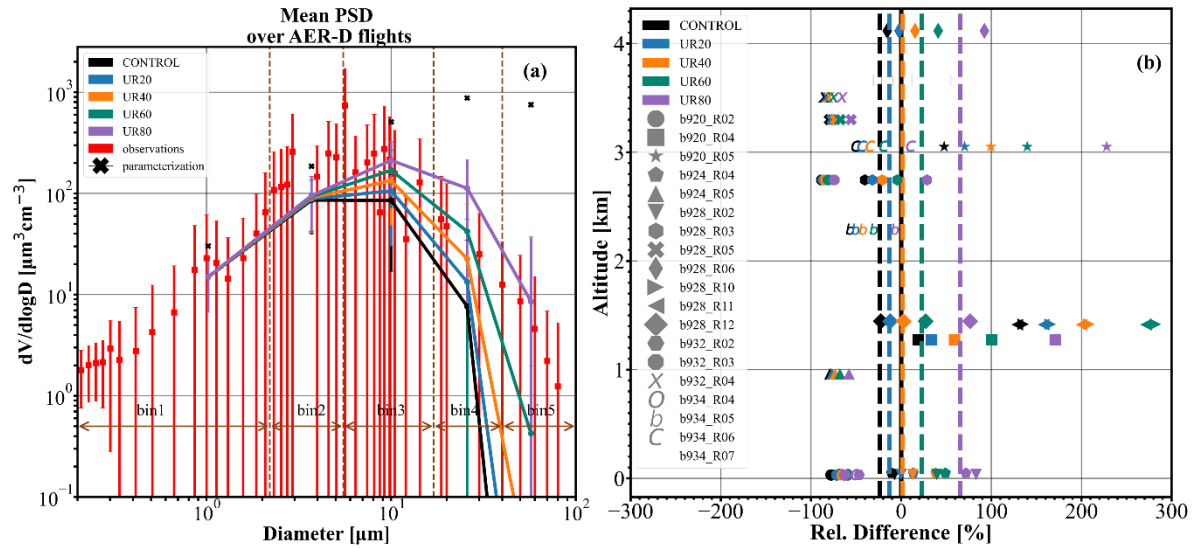
930

931

932

933

Figure 7: Modeled and observed dust PSD of flight b928, for straight-level-runs (a) R02, (b) R03, (c) R05, (d) R06, (e) R10, (f) R11 and (g) R12. The in situ observations are shown with red squares (along with the total instrumentation error). The collocated modeled PSDs are shown with lines, for the CONTROL run (black), UR20 (blue), UR40 (orange), UR60 (green), and UR80 (purple) and the corresponding standard deviation with the associated error bars. The brown vertical lines indicate the limits of the model size bins. The inlet maps show the flight segment track and the collocated model grid points.



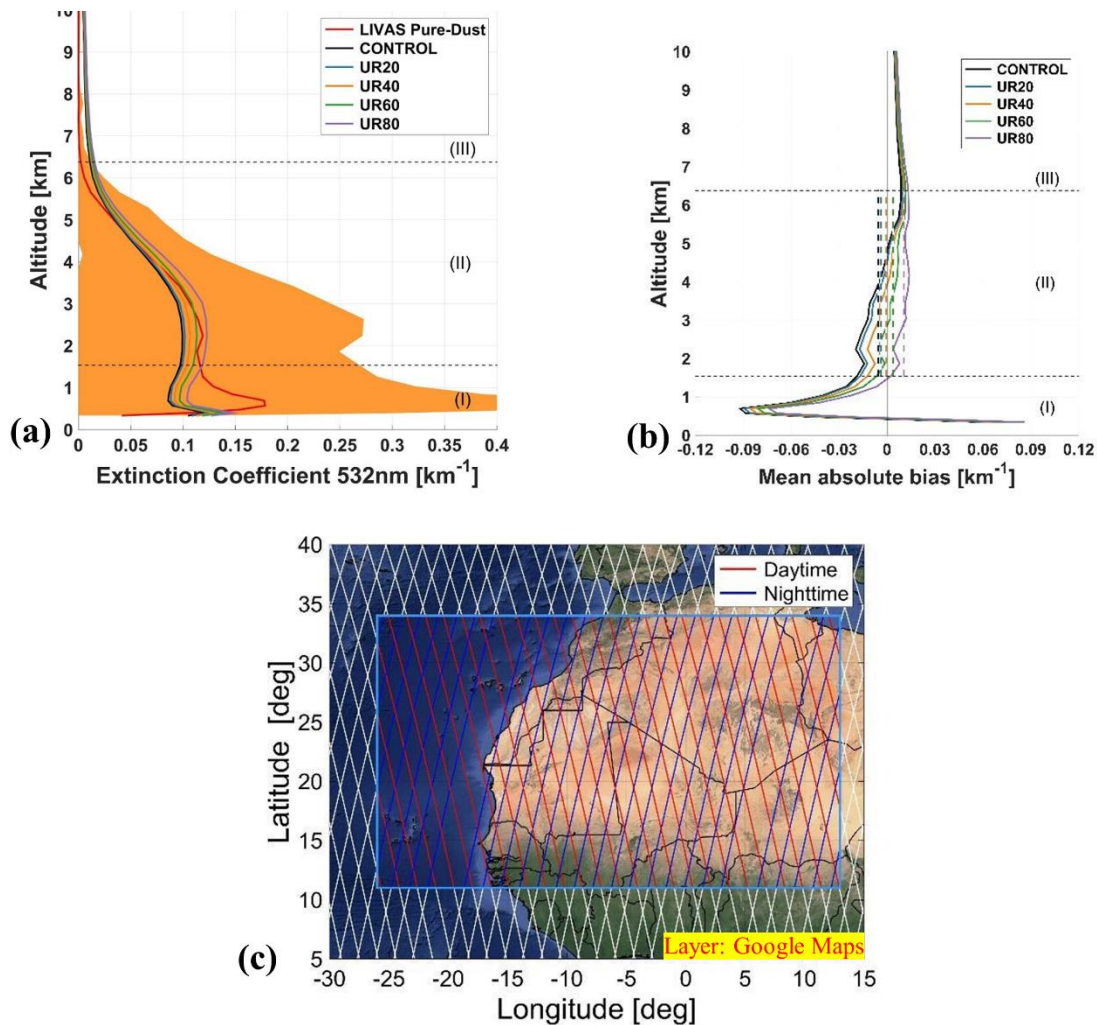
935

936

Figure 8: (a) Mean PSD of AER-D/ICE-D campaign. The observations are shown with red squares, whereas the simulations are shown with solid lines for the CONTROL run (black), UR20 (blue), UR40 (orange), UR60 (green), and UR80 (purple). (b) The relative difference between the observations and the model simulations of the total volume of dust particles, at different altitudes. The observations from different flight segments (i.e., b920 R02, b920 R04, b920 R05, b924 R04, b924 R05, b928 R03, b928 R05, b928 R06, b932 R02, b932 R03, b932 R04, b934 R04, b934 R05, b934 R06, and b934 R07) are denoted with different markers. The average relative difference of the observations and the simulations are denoted with dashed lines, for the CONTROL run (black), UR20 (blue), UR40 (orange), UR60 (green), and UR80 (purple).

944

945



946
 947 **Figure 9: (a) Profile of the mean extinction coefficient at 532 nm, by LIVAS pure-dust product (black red line), and**
 948 **profiles of the mean extinction coefficient at 532 nm simulated from the different experiments of Table 3 (CONTROL,**
 949 **UR20/40/60/80).** The orange shading indicates the standard deviation of the LIVAS profile averaging. (b) The mean
 950 mean absolute biases between the LIVAS profile and the simulated profiles from the different experiments, in the domain of
 951 interest, between 05/08/2015 and 25/08/2015. The vertical dashed lines are the mean absolute bias between the LIVAS
 952 profile and the simulated profiles from the different experiments averaged over the altitudes of region II. (c) The
 953 domain of interest and the daytime (red) and nighttime (blue) CALIPSO overpasses. The vertical dashed lines are the
 954 mean absolute bias between the LIVAS profile and the simulated profiles from the different experiments averaged over
 955 the altitudes of region II. Layer: google maps background.

958 **Table 1 Size ranges and properties of model size bins in the default WRF-GOCART-AFWA scheme**

WRF-GOCART-AFWA					
Bins	1	2	3	4	5
$D_{lo} - D_u$ (μm)	0.2-2.0	2.0-3.6	3.6-6.0	6.0-12.0	12.0-20.0
D_{eff} (μm)	1.46	2.8	4.8	9.0	16.0
ρ_p (g cm^{-3})	2.5	2.65	2.65	2.65	2.65
WRF-L					
Bins	1	2	3	4	5
$D_{lo} - D_u$ (μm)	0.2-2.2	2.2-5.5	5.5-17.0	17.0-40.0	40.0-100.0
D_{eff} (μm)	1.02	3.7	10.0	25.8	57.2
ρ_p (g cm^{-3})	2.5	2.65	2.65	2.65	2.65

959
960 **Table 2 Configuration parameters of the WRF-L runs**

Parameterization	Scheme	Parameterization	Scheme
Surface Model	Noah (Chen and Dudhia, 2001)	sf_surface_physics	2
Surface Layer	Monin-Obukov-Janjic (Janić, 2001)	sf_sfclay_physics	2
Radiation (SW and LW)	RRTMG (Iacono et al., 2008)	ra_sw(lw)_physics	4
Microphysics	Morrison 2-moment (Morrison et al., 2005)	mp_physics	10
Cumulus	Grell-3 (Grell and Dévényi, 2002)	cu_physics	5
Boundary Layer	MYNN 2.5 (Nakanishi and Niino, 2006)	bl_pbl_physics	5
Chemistry	GOCART simple (Ginoux et al., 2001; LeGrand et al., 2019)	chem_opt	300
Dust Scheme	AFWA (LeGrand et al., 2019)	dust_opt	3

961 **Table 3 Experimental runs that performed in this study**

Experiment	Code
CONTROL	WRF-L
UR20	WRF-L with reduced settling velocities by 20% of their settling velocity
UR40	WRF-L with reduced settling velocities by 40% of their settling velocity
UR60	WRF-L with reduced settling velocities by 60% of their settling velocity
UR80	WRF-L with reduced settling velocities by 80% of their settling velocity

962 **Table 4: Lognormal** $\left(\frac{dV}{d\ln D} = \frac{V_{tot}}{\sqrt{2\pi}\ln\sigma_g} \exp\left(-\frac{(\ln D_v - \ln D)^2}{2(\ln\sigma_g)^2}\right)\right)$ **mode parameters of the fitted FENNEC-PSD. Diameters are**
 963 **given in $[\mu m]$ and volume concentrations in $[\frac{\mu m^3}{cm^3}]$:**

Modes	1	2	3	4	5
V_{tot}	15.16	27.07	169.32	310.5	563.3
D_v	1.0	2.5	7.0	22.0	50.0
s_g	1.8	2.0	1.9	2.0	2.15

964